The *Drosophila* chemokine-like Orion bridges phosphatidylserine and Draper in phagocytosis of neurons

Hui Ji[1], Bei Wang[1], David Labib[1,3], Joyce Lei[1,4], Xinchen Chen[1], Maria Sapar[1,3], Ana Boulanger[2], Jean-Maurice Dura[2] and Chun Han[1,*]

[1]Weill Institute for Cell and Molecular Biology and Department of Molecular Biology and Genetics, Cornell University, Ithaca, NY 14853, USA

[2] IGH, Univ Montpellier, CNRS, Montpellier, France

[3]Current address: The New York Stem Cell Foundation Research Institute, New York, NY 10019, USA

[4]Current address: Tisch MS Research Center of New York, New York, NY 10019, USA

[*]Correspondence: chun.han@cornell.edu

RUNNING TITLE

Orion bridges PS and Drpr in neuronal phagocytosis

ABSTRACT

Phagocytic clearance of degenerating neurons is triggered by "eat-me" signals exposed on the neuronal surface. The conserved neuronal eat-me signal phosphatidylserine (PS) and the engulfment receptor Draper (Drpr) mediate phagocytosis of degenerating neurons in *Drosophila*. However, how PS is recognized by Drpr-expressing phagocytes *in vivo* remains poorly understood. Using multiple models of dendrite degeneration, we show that the *Drosophila* chemokine-like protein Orion is a PS-binding protein responsible for detecting PS exposure on neurons; it is supplied cell-non-autonomously to coat PS-exposing dendrites and to bridge interactions between PS and Drpr, thus enabling phagocytosis. As a result, the accumulation of Orion on neurons and on phagocytes produces opposite outcomes by potentiating and suppressing phagocytosis, respectively. Moreover, the Orion dosage is a key determinant of the sensitivity of phagocytes to PS exposed on neurons. Lastly, mutagenesis analyses show that the sequence motifs shared between Orion and human immunomodulatory proteins are important for Orion secretion and binding to PS. Thus, our results uncover a missing link in PS-mediated phagocytosis in *Drosophila* and imply conserved mechanisms of phagocytosis of neurons.

KEYWORDS

phosphatidylserine, phagocytosis, da neurons, epidermal cells, Orion, Draper, CX_3C, RRY, bridging molecule

INTRODUCTION

Phagocytosis of apoptotic and degenerative neurons is essential for the development and homeostasis of the nervous system (Frost and Schafer, 2016; Galloway et al., 2019). Abnormal phagocytosis is also associated with neuroinflammation and neurodegenerative diseases (Salter and Stevens, 2017). Neuronal debris is recognized and cleared by resident phagocytes of the nervous system through "eat-me" signals exposed on the neuronal surface. A conserved "eat-me" signal is phosphatidylserine (PS), a negatively charged phospholipid normally kept in the inner leaflet of the plasma membrane by P4-ATPase flippases (Leventis and Grinstein, 2010). During neurite degeneration and apoptosis, PS is externalized to the outer surface of neuronal membranes (Nagata, 2018; Sapar et al., 2018; Shacham-Silverberg et al., 2018; Sievers et al., 2003). Exposed PS dominantly triggers phagocytosis of neurons, as demonstrated by the observation that loss of PS flippases in neurons results in PS exposure and neurodegeneration across species (Darland-Ransom et al., 2008; Sapar et al., 2018; Zhu et al., 2012). Besides clearing existing neuronal debris, PS-mediated phagocytosis also drives the degeneration of injured neurites and neurons with certain genetic perturbations (Ji et al., 2022; Sapar et al., 2018). In the central nervous system (CNS), local PS exposure enables microglia-mediated synaptic elimination (Li et al., 2020; Park et al., 2021; Scott-Hewitt et al., 2020). Thus, the regulation and recognition of neuronal PS exposure are critical for the development and homeostasis of the nervous system.

52 *Drosophila* has been an important model organism for studying neuronal phagocytosis. In
53 *Drosophila*, Draper (Drpr) is the best-known receptor responsible for phagocytosis of neurons
54 (Freeman et al., 2003). As a homolog of the *C. elegans* engulfment receptor CED-1 (Zhou et al.,
55 2001) and the mammalian engulfment receptors Jedi-1 and MEGF10 (Wu et al., 2009), Drpr is
56 involved in many contexts of neuronal phagocytosis, including the clearance of apoptotic
57 neurons during embryonic development (Freeman et al., 2003; Tung et al., 2013), axon and
58 dendrite pruning during neuronal remodeling (Awasaki et al., 2006; Williams et al., 2006),
59 injury-induced neurite degeneration (MacDonald et al., 2006; Tao and Rolls, 2011), and removal
60 of destabilized boutons at neuromuscular junctions (Fuentes-Medel et al., 2009). Neurons with
61 ectopic PS exposure are engulfed by phagocytes in a Drpr-dependent manner (Ji et al., 2022;
62 Sapar et al., 2018), suggesting that Drpr is critical for PS sensing. The observation that the
63 extracellular domain of Drpr can bind to PS *in vitro* further suggests that Drpr is a PS receptor
64 (Tung et al., 2013). However, whether Drpr directly recognizes PS exposed on neurons *in vivo* is
65 still unknown. In addition, while detection of PS by diffusible PS sensors is common in other
66 species (Hanayama et al., 2002; Wang et al., 2010), to date, no such diffusible PS sensors have
67 been identified in *Drosophila*.

68 Recently, the secreted protein Orion was discovered as being required for the
69 developmental pruning and clearance of *Drosophila* mushroom body (MB) axons (Boulanger et
70 al., 2021). Orion is expressed by MB neurons and is required for astrocytes to infiltrate axon
71 bundles and engulf axonal debris. Interestingly, Orion shares a CX_3C motif with mammalian
72 CX3CL1 (also known as fractalkine), which is required for the elimination of synapses in the
73 mouse barrel cortex (Gunner et al., 2019). CX3CL1 is known as a chemokine because of its
74 ability to direct migration of leukocytes and microglia (Bazan et al., 1997; Maciejewski-Lenoir
75 et al., 1999). Thus, Orion represents the first known chemokine-like molecule in *Drosophila* and
76 shares conserved functions with CX3CL1 in the remodeling of the nervous system. However,
77 how Orion and CX3CL1 exactly function in the phagocytosis of neurons is still unknown.

78 In this study, we examined Orion's function in the phagocytosis of *Drosophila* class IV
79 dendritic arborization (C4da) neurons, a well-established *in vivo* model for studying PS-mediated
80 phagocytosis (Han et al., 2014; Ji et al., 2022; Sapar et al., 2018). C4da neurons grow elaborate
81 sensory dendrites on larval epidermal cells (Han et al., 2012), which act as the primary
82 phagocytes during dendrite degeneration and remodeling (Han et al., 2014). Ectopically induced
83 PS exposure on C4da neurons due to loss of P4-ATPase flippases causes dendrite membrane loss
84 in a Drpr-dependent manner (Sapar et al., 2018). PS exposure and phagocytosis-driven dendrite
85 degeneration can also be induced by injury and by removing the NAD^+-producing enzyme
86 Nmnat (Ji et al., 2022), since normal PS asymmetry on the dendrite membrane depends on
87 sufficient NAD^+ levels in the neuron (Sapar et al., 2018; Shacham-Silverberg et al., 2018).

88 Here we present *in vivo* evidence that, instead of being a direct PS receptor, Drpr relies
89 on Orion as a PS-binding bridging molecule to sense PS on neurons. Orion is secreted by
90 peripheral non-neural tissues and serves as a non-autonomous permissive factor for phagocytosis

91 of neurons. Orion binds to PS on neurons and is also enriched on phagocytes over-expressing
92 Drpr. Strikingly, a membrane-tethered Orion expressed by neurons dominantly induces
93 phagocytosis even in the absence of PS exposure, while Orion accumulation on the surface of
94 phagocytes makes phagocytes blind to PS-exposing neurons. Importantly, the dosage of Orion
95 determines the sensitivity of phagocytes to neuronal PS exposure. Lastly, we establish that the
96 motifs Orion shares with human chemokines and neutrophil peptides are critical for PS binding
97 and protein secretion. These findings reveal key mechanisms of PS recognition in *Drosophila*
98 and imply potentially conserved roles of chemokines in PS-mediated phagocytosis of neurons.

99 **RESULTS**

100 ***orion* is required for phagocytosis of dendrites**

101 To determine if *orion* is involved in phagocytosis of degenerating dendrites of da neurons, we
102 first examined phagocytosis of injured dendrites in the *orion*^{1} mutant, which results in a G to D
103 mutation in the C-termini of both Orion protein isoforms (Figure 1—figure supplement 1A) and
104 abolishes clearance of pruned axons during MB remodeling (Boulanger et al., 2021). Dendrites
105 were severed from the cell body using laser, and engulfment of the injured dendrites was
106 visualized using MApHS, a pH-sensitive dendritic marker consisting of extracellular pHluorin
107 and intracellular tdTom (Han et al., 2014). Engulfment was signified by the loss of pHluorin
108 signal due to the drop of pH in early phagosomes (Botelho and Grinstein, 2011; Han et al.,
109 2014). Injured dendrites of C4da neurons in the control larvae were completely engulfed by
110 epidermal cells 24 hours (hrs) after injury (AI), as indicated by the loss of pHluorin signals on
111 tdTom-positive dendritic debris dispersed in epidermal cells (Figures 1A-1A", and 1D). Because
112 *orion* is located on the X chromosome, we examined both hemizygous male larvae and
113 homozygous female larvae of *orion*^{1}. In contrast to the wildtype (WT), both groups of *orion*^{1}
114 mutants showed little engulfment of injured dendrites by epidermal cells (Figures 1B-1C", and
115 1D), as indicated by the presence of pHluorin signals on tdTom-labeled debris of injured
116 dendrites. The debris remained in the original dendritic patterns, which is another sign of
117 impaired engulfment by epidermal cells. These results suggest that *orion* is required for the
118 engulfment of injured dendrites. Since male and female *orion* mutants exhibited similar degrees
119 of engulfment defects (Figure 1D), we used hemizygous male mutants only in subsequent assays.

120 In addition to phagocytosis after injury, C4da dendrites are all pruned and engulfed by
121 epidermal cells during metamorphosis (Han et al., 2014). Consistent with the role of *orion* in
122 axonal pruning of MB neurons (Boulanger et al., 2021), we also confirmed that *orion*^{1} exhibits
123 strong defects in the clearance of pruned dendrites of C4da neurons during metamorphosis
124 (Figure 1—figure supplement 1B-1D).

125 The engulfment of injured dendrites by epidermal cells is mediated by PS exposure on
126 dendrites (Ji et al., 2022; Sapar et al., 2018). To test directly if *orion* is required for PS exposure-
127 induced phagocytosis, we examined two additional paradigms in which PS exposure can be more
128 reliably induced and studied. In the first paradigm, PS exposure was ectopically induced in

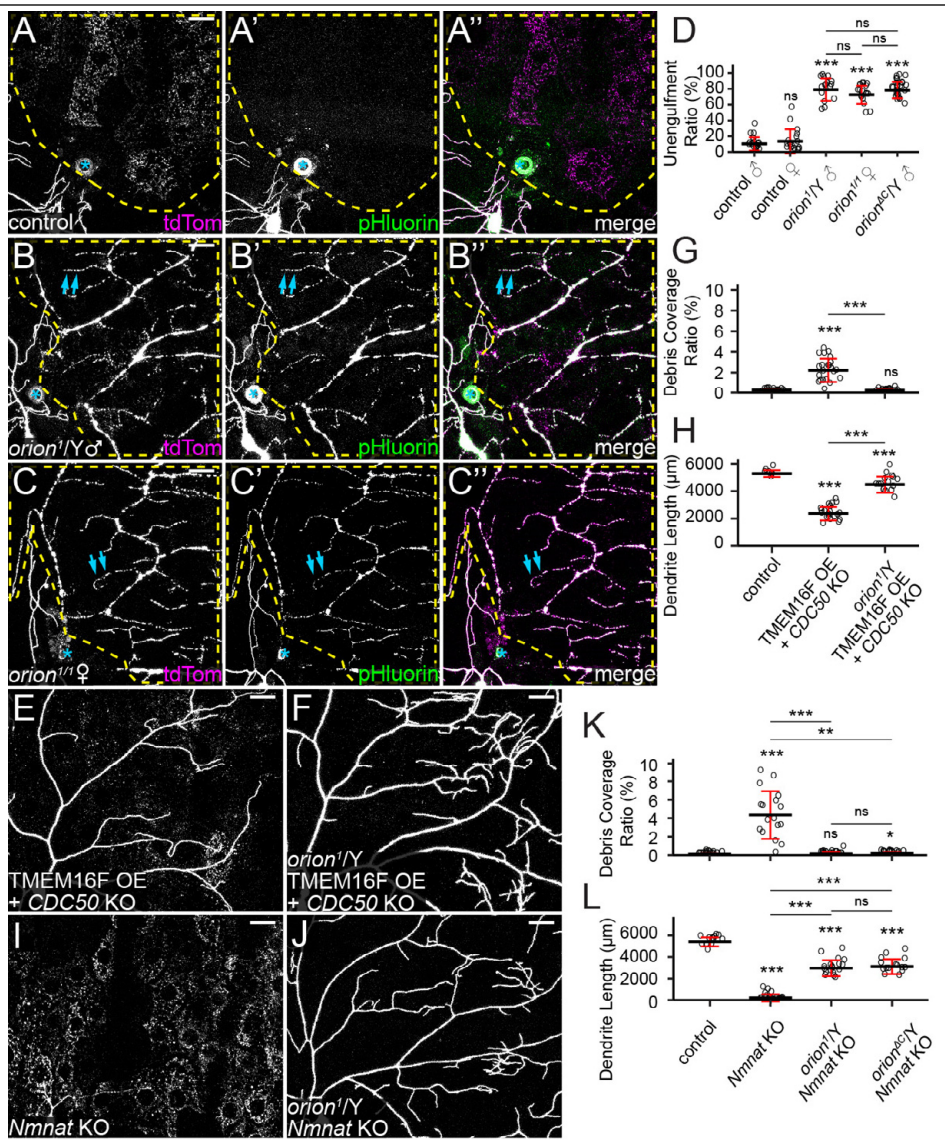

Figure 1: *orion* is required for phagocytosis of dendrites in multiple dendrite degeneration paradigms

(A-C") Partial dendritic fields of ddaC neurons in control (A-A"), *orion*^{1} hemizygous (B-B"), and *orion*^{1} homozygous (C-C") larvae at 22-24 hrs after injury (AI). Yellow dash outlines: territories originally covered by injured dendrites; blue asterisks: injury sites; blue arrows: injured but unengulfed dendrite fragments.

(D) Quantification of unengulfment ratio of injured dendrites (pHluorin-positive debris area/tdTom-positive debris area). n = number of neurons: control males (n = 18, 10 animals); control females (n = 16, 9 animals); *orion*^{1}/Y (n = 16, 8 animals); *orion*$^{1/1}$ (n = 18, 9 animals); *orion*$^{\Delta C}$/Y (n = 25, 12 animals). One-way ANOVA and Tukey's test. (E and F) Partial dendritic fields of TMEM16F OE + CDC50 KO neurons in the wildtype background (E) and orion1 hemizygous background (F).

(G and H) Quantification of debris coverage ratio (percentage of debris area normalized by dendrite area) (G) and dendrite length (H) at 140 hrs after egg laying (AEL). n = number of neurons: control (n = 14, 7 animals); TMEM16F OE + CDC50 KO (n = 22, 11 animals); TMEM16F OE + CDC50 KO in orion1/Y (n = 16, 8 animals). For (G), Kruskal-Wallis (One-way ANOVA on ranks) and Dunn's test, p-values adjusted with the Benjamini-Hochberg method; for (H), One-way ANOVA and Tukey's test.

(I and J) Partial dendritic fields of Nmnat KO neurons in the wildtype background (I) and orion1 hemizygous background (J).

(K and L) Quantification of debris coverage ratio (K) and dendrite length (L) at 120 hrs AEL. n = number of neurons: control (n = 17, 9 animals); Nmnat KO (n = 17, 9 animals); Nmnat KO in orion1/Y (n = 18, 9 animals); Nmnat KO in orionΔC/Y, (n = 16, 9 animals). For (K), Kruskal-Wallis (One-way ANOVA on ranks) and Dunn's test, p-values adjusted with the Benjamini-Hochberg method; for (L), One-way ANOVA and Tukey's test.

In all image panels, neurons were labeled by ppk-MApHS. Scale bars, 25 µm. For all quantifications, *p≤0.05, **p≤0.01, ***p≤0.001; n.s., not significant. The significance level above each genotype is for comparison with the control. Black bar, mean; red bar, SD. See also Figure 1—figure supplement 1.

129 otherwise healthy neurons using a combination of *CDC50* knockout (KO) and TMEM16F

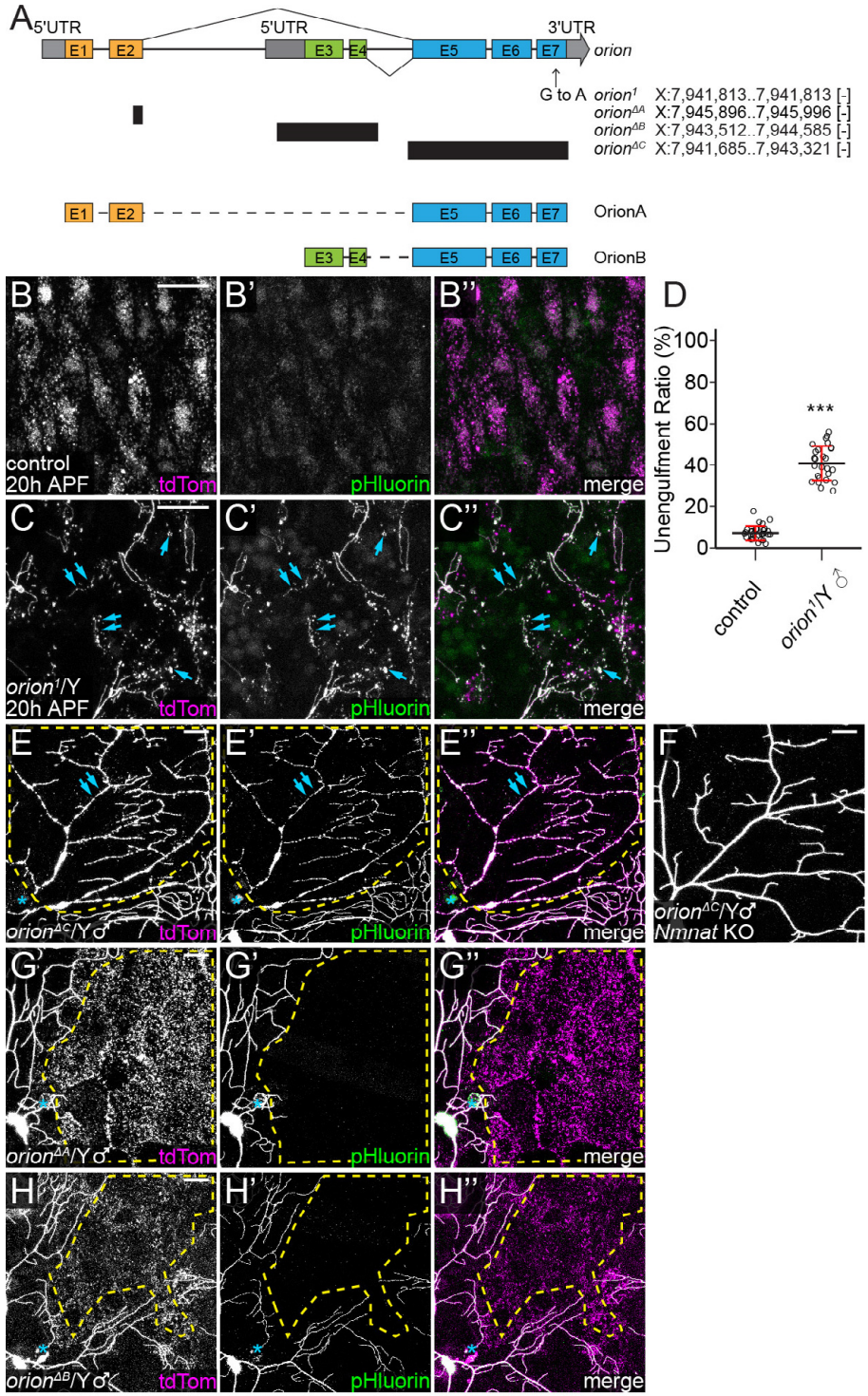

Figure 1—figure supplement 1: *orion* mutant alleles and engulfment phenotypes

(A) Schematic representation of the *orion* locus in the wildtype and in four different *orion* alleles (*orion*^{1}, *orion*$^{\Delta A}$, *orion*$^{\Delta B}$ and *orion*$^{\Delta C}$). Black bars indicate deleted regions. The two mRNA splicing isoforms of *orion* are also indicated. The *orion* gene annotation is based on Release 6 reference genome assembly.

(B-C") Partial dendritic fields of ddaC neurons at 20 hrs after puparium formation (APF) in wildtype (B-B") and *orion*^{1} hemizygous (C-C") pupae. Blue arrows: unengulfed dendrite fragments.

(D) Quantification of unengulfment ratio of pruned dendrites (area of pHluorin-positive debris/area of tdTom-positive debris) at 19-21 hrs APF. n = number of neurons: control (n = 30, 12 animals); *orion*^{1} hemizygotes (n = 26, 9 animals). Welch's t-test; ***p≤0.001; black bar, mean; red bars, SD.

(E-E") Partial dendritic field of a ddaC neuron in *orion*$^{\Delta C}$ hemizygotes at 23 hrs AI. Blue arrows: injured but unengulfed dendrite fragments.

(F) Partial dendritic field of a *Nmnat* KO neuron in *orion*$^{\Delta C}$ hemizygotes.

(G-H") Partial dendritic fields of ddaC neurons in *orion*$^{\Delta A}$ hemizygotes (G-G"), and *orion*$^{\Delta B}$ hemizygotes (H-H") at 23-24 hrs AI.

In all image panels, neurons were labeled by *ppk-MApHS*. Scale bars, 25 μm. In (E-E") and (G-H"), yellow dash outlines: territories originally covered by injured dendrites; blue asterisks: injury sites.

130 overexpression (OE). *CDC50* encodes a chaperone protein required for the activity of P4-

131 ATPases that keep PS in the inner leaflet of the plasma membrane (Segawa and Nagata, 2015).
132 TMEM16F is a mammalian scramblase that mixes PS between the two leaflets of the plasma
133 membrane (Nagata et al., 2016; Suzuki et al., 2010). Dendrites with *CDC50* KO and TMEM16F
134 OE expose PS and shed membrane in a phagocytosis-dependent manner (Sapar et al., 2018).
135 Whereas these neurons showed reduced dendrite length and elevated debris levels in wandering
136 3rd instar larvae with wildtype *orion* (Figures 1E, 1G, and 1H), *orion*^{1} hemizygous males
137 exhibited almost normal dendritic length and no dendritic debris in epidermal cells (Figures 1F-
138 1H), indicating a lack of engulfment by phagocytes.

139 In the second paradigm, we knocked out *Nmnat* to induce dendritic PS exposure and
140 phagocytosis-dependent dendrite degeneration (Ji et al., 2022). *Nmnat* encodes an enzyme
141 involved in the biosynthesis of NAD^+, protecting neurites from degeneration (Zhai et al., 2009).
142 The loss of *Nmnat* in C4da neurons results in PS exposure and phagocytosis-dependent dendrite
143 degeneration, likely due to NAD^+ reduction (Ji et al., 2022). *Nmnat* KO neurons lost most of
144 their dendrites and showed widespread debris in epidermal cells at 120 hrs after egg laying
145 (AEL) (Ji et al., 2022)(Figures 1I, IK, and 1L). In contrast, resembling *drpr* loss-of-function
146 (LOF) (Ji et al., 2022), *orion*^{1} hemizygosity completely rescued the dendrite degeneration of
147 *Nmnat* KO neurons, as indicated by the absence of dendrite debris (Figures 1J-IK). The dendrite
148 length of these neurons was restored to 53% of the WT level (Figures 1I-IL), suggesting that
149 Nmnat may also be involved in dendrite growth or maintenance. Altogether, above data indicate
150 that *orion* is required for PS-mediated phagocytosis of dendrites by epidermal cells.

151 Because *orion*^{1} carries a missense mutation that may not completely abolish Orion
152 function, we compared its properties to those of *orion*$^{\Delta C}$, a predicted null mutation that is missing
153 all three common C-terminal exons of both *orion* isoforms (Figure 1—figure supplement 1A)
154 (Boulanger et al., 2021). *orion*$^{\Delta C}$ showed similar levels of phagocytosis defects as *orion*^{1} in both
155 injury-induced degeneration (Figure 1—figure supplement 1E-1E", and Figure 1D) and *Nmnat*
156 KO-induced degeneration (Figure 1—figure supplement 1F, and Figure 1K-1L), suggesting that
157 *orion*^{1} has lost most, if not all, of its function (we show later that the Orion^{1} protein has weak
158 activities that can be observed in extremely sensitive assays with overexpressed mutant protein).
159 Since *orion* encodes two isoforms with different N-terminal sequences (Figure 1—figure
160 supplement 1A), we next asked if one or both isoforms contribute to phagocytosis. Mutations
161 targeting each of the two *orion* isoforms separately (Figure 1—figure supplement 1A) showed no
162 phagocytosis defects in injury-induced degeneration (Figure 1—figure supplement 1G-1H"),
163 suggesting that OrionA and OrionB isoforms are redundant in the phagocytosis of injured
164 dendrites. These results are consistent with the redundant effects of the same mutations in MB
165 neuron axon pruning (Boulanger et al., 2021).

166 **Orion functions cell-non-autonomously**

167 *orion* encodes a secreted protein, raising the question of how it contributes to phagocytosis of
168 dendrites. To determine which tissues express Orion, we generated an *orion* knock-in (KI) allele
169 in which the C-terminus of *orion* is fused in-frame with 4 copies of mNeonGreen2$_{11}$ (mNG2$_{11}$)

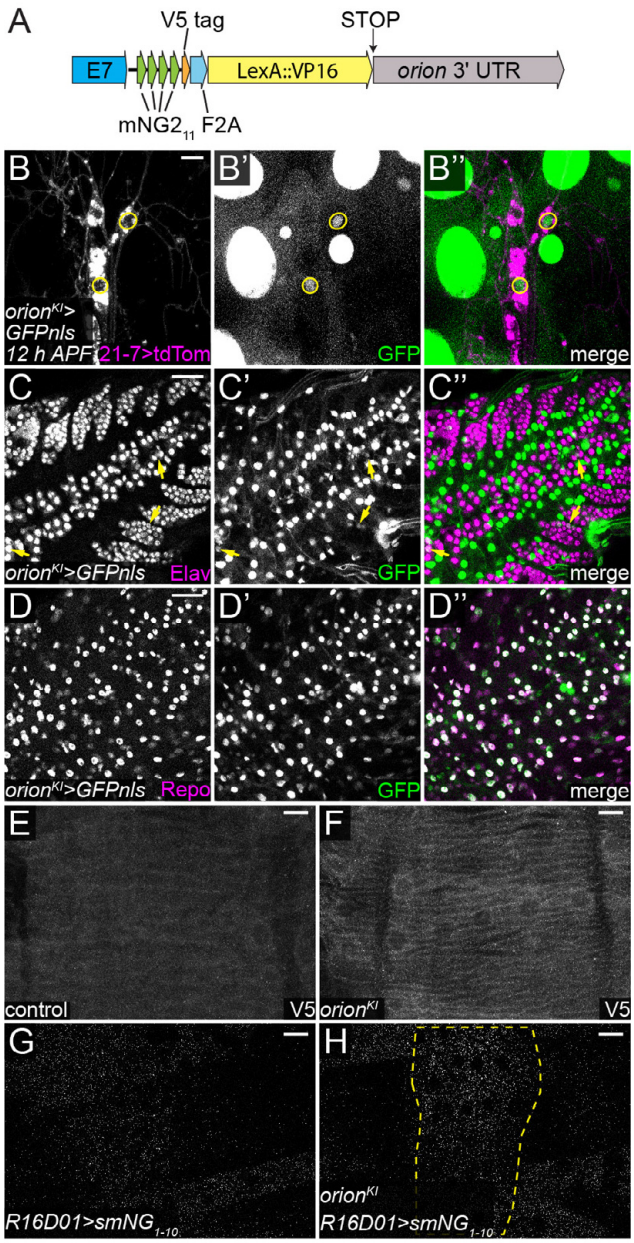

Figure 2—figure supplement 1: Orion functions cell-non-autonomously

(A) Schematic representation of the *orion*^{KI} allele.

(B-B") GFPnls expression driven by *orion-LexA* in ddaC and ddaE neurons at 12 hrs APF. Yellow circles indicate nuclei of ddaC and ddaE neurons. Neurons were labeled by *21-7-Gal4>CD4-tdTom*.

(C-D") GFPnls expression driven by *orion-LexA* in the larval ventral nerve cord (VNC). Nuclei of neurons are labeled by Elav staining (C-C"); glial nuclei are labeled by Repo staining (D-D"). Yellow arrows (C-C"): a small number of neurons expressing *orion*.

(E-F) V5 staining of larval body walls in the wildtype control (w^{1118}) (E) and *orion*^{KI} (F).

(G-H) Signals of reconstituted mNG in control (G) and *orion*^{KI} (H) epidermal cells. Secreted mNG$_{1-10}$ (smNG$_{1-10}$) was expressed in patches of epidermal cells (outlined in H) driven by *R16D01-Gal4*.

Scale bars, 10 μm (B) and 25 μm (C-H).

(Feng et al., 2017), a V5 tag, a self-cleaving F2A sequence (Szymczak et al., 2004), and LexA::VP16 (Chen et al., 2014) (Figure 2—figure supplement 1A). This allele, abbreviated as *orion*^{KI}, has several purposes: detection of *orion*-expressing cells by LexA::VP16 transcription activity, detection of endogenous Orion proteins by V5 staining, and visualization of endogenous Orion proteins in a tissue-specific manner by reconstitution of mNG2 fluorescence with tissue-specific expression of mNG2$_{1-10}$ (Feng et al., 2017).

By using *orion*^{KI} with a *LexAop-GFPnls* reporter, we found that *orion* transcripts are expressed in many peripheral tissues in larvae, including epidermal cells, hemocytes, trachea, and the fat body (Figure 2A-2B). However, *orion* transcription is missing in larval da neurons (Figure 2A, inset), even though a weak *orion* transcription activity was later detected in a subset

of da neurons at 5-12 hrs after puparium formation (APF) (Figure 2—figure supplement 1B-1B"), when some da neurons die and others undergo dendritic pruning (Williams and Truman, 2005a). In the central nervous system, we found that *orion* was transcribed in most glial cells and in a small subset of neurons at the wandering 3rd instar larval stage (Figure 2—figure supplement

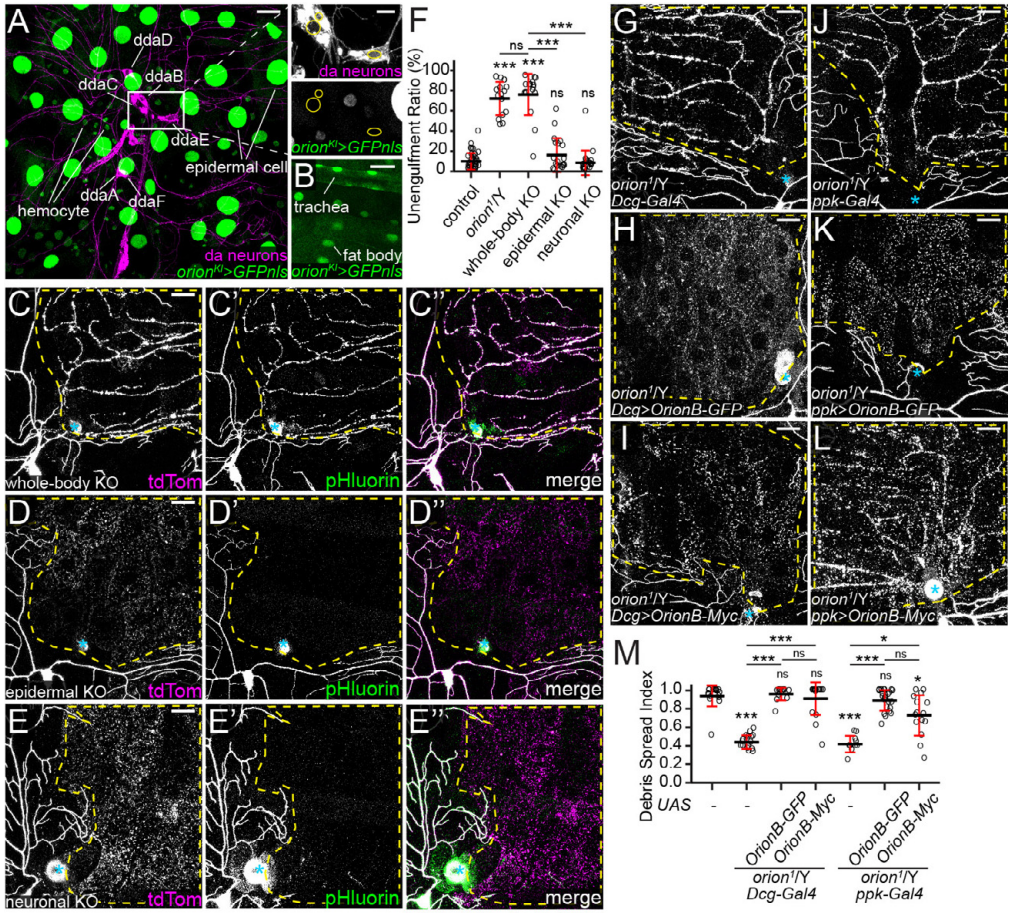

Figure 2: Orion functions cell-non-autonomously

(A-B) GFPnls expression driven by *orion-LexA* (*orion*^{KI}) in epidermal cells, hemocytes (A), trachea, and fat body (B), but not in da neurons (A, insets). Yellow circles indicate nuclei of ddaB, ddaC, and ddaE neurons (A). Scale bars, 25 µm (A), 10 µm (A insets), and 50 µm (B).

(C-E") Partial dendritic fields of neurons in whole-body *orion* KO (C-C"), epidermal *orion* KO (D-D"), and neuronal *orion* KO (E-E") at 22-24 hrs AI.

(F) Quantification of unengulfment ratio of injured dendrites. n = number of neurons: control and *orion*^{1}/Y (same dataset as in Figure 1D); whole-body *orion* KO (n = 18, 10 animals); epidermal *orion* KO (n = 19, 11 animals); neuronal *orion* KO (n = 21, 11 animals). One-way ANOVA and Tukey's test.

(G-L) Partial dendritic fields of ddaC neurons in *orion*^{1} hemizygotes with fat body Gal4 (G), with OrionB-GFP OE in the fat body (H), with OrionB-Myc OE in the fat body (I), with neuron Gal4 (J), with OrionB-GFP OE in neurons (K), and with OrionB-Myc OE in neurons (L) at 22-24 hrs AI.

(M) Quantification of debris spread index of injured dendrites (area ratio of all 15 pixel x 15 pixel squares that contained dendrite debris in the region of interest). n = number of neurons: wildtype control (n = 18, 10 animals); *Dcg-Gal4* in *orion*^{1}/Y (n = 16, 9 animals); *Dcg>OrionB-GFP* in *orion*^{1}/Y (n = 13, 7 animals), *Dcg>OrionB-Myc* in *orion*^{1}/Y (n = 17, 10 animals); *ppk-Gal4* in *orion*^{1}/Y (n = 10, 6 animals); *ppk>OrionB-GFP* in *orion*^{1}/Y (n = 24, 12 animals); *ppk>OrionB-Myc* in *orion*^{1}/Y (n = 15, 9 animals). Kruskal-Wallis (One-way ANOVA on ranks) and Dunn's test, p-values adjusted with the Benjamini-Hochberg method.

Neurons were labeled by *21-7>UAS-CD4-tdTom* (A-B), *ppk-MApHS* (C-E"), *ppk-CD4-tdTom* (G, H, I), and *ppk>CD4-tdTom* (J, K, L). In (C-E") and (G-L), yellow dash outlines: territories originally covered by injured dendrites; blue asterisks: injury sites; scale bars, 25 µm. For all quantifications, *p≤0.05, ***p≤0.001; n.s., not significant. The significance level above each genotype is for comparison with the control. Black bar, mean; red bar, SD. See also Figure 2—figure supplement 1.

184 1C-1D"). Despite the robust LexA::VP16 activity in *orion*^{KI}, Orion proteins appear to be
185 expressed at a low level. Using V5 staining, we could observe only weak Orion signals on the
186 larval epidermis (Figure 2—figure supplement 1E and 1F). By expressing secreted mNG2$_{1-10}$ in a
187 patch of epidermal cells (in the R16D01 domain), we also detected weak Orion-mNG2 signals in
188 what appear to be the secretory compartments of epidermal cells (Figure 2—figure supplement
189 1G and 1H).

190 To investigate whether *orion* is required in specific tissues for phagocytosis of injured
191 dendrites, we knocked out *orion* in either neurons or epidermal cells using CRISPR-TRiM, a
192 method of tissue-specific mutagenesis that relies on a tissue-specific Cas9 and ubiquitously
193 expressed guide RNAs (gRNAs) (Poe et al., 2019). As a control, knocking out *orion* with a
194 ubiquitous Cas9 (*Act5C-Cas9*) (Port et al., 2014) faithfully replicated the phagocytosis defects of
195 *orion*^{1} (Figures 2C-2C", and 2F), demonstrating the effectiveness of CRISPR-TRiM. However,
196 *orion* KO in either da neurons alone (with *SOP-Cas9*; (Poe et al., 2019)) or in epidermal cells
197 alone (with *shot-Cas9*; (Ji et al., 2022)) did not interfere with the engulfment of injured dendrites
198 (Figures 2D-2E", and 2F).

199 The lack of effect of *orion* KO in da neurons or in epidermal cells suggests that Orion
200 functions cell-non-autonomously. We further tested this idea by asking whether supplying Orion
201 in the extracellular space is sufficient to rescue the impaired engulfment of injured dendrites in
202 *orion* mutants. Extracellular Orion supply was achieved by overexpressing Orion in the fat body,
203 which can efficiently secrete proteins into the hemolymph (Sapar et al., 2018). We quantified the
204 degree of engulfment by the spread of dendrite debris in the epidermis: Successful engulfment
205 will cause an even dispersion of the debris whereas failure of engulfment will result in dendrite
206 fragments remaining in the original dendrite pattern. Because overexpression (OE) of OrionA in
207 the fat body caused early larval lethality, we chose to use two OrionB transgenes in these rescue
208 experiments: one tagged with Myc constructed in an intermediate-expression vector (Boulanger
209 et al., 2021), and the other tagged with GFP constructed in a high-expression vector (Sapar et al.,
210 2018). Both OrionB transgenes overexpressed in the fat body rescued the engulfment of injured
211 dendrites in *orion*^{1} hemizygotes to the wildtype level (Figures 2G-2I, and 2M).

212 We next checked whether OrionB secreted from neurons is sufficient to rescue the
213 engulfment defects in the *orion*^{1} mutant. Interestingly, neuronal expression of OrionB-GFP fully
214 rescued the engulfment defects (Figure 2K, and 2M), while OrionB-Myc did not rescue
215 engulfment to the wildtype level (Figure 2L, and 2M), consistent with the predicted higher
216 expression of OrionB-GFP.

217 Together, these results indicate that Orion is primarily expressed in non-neural tissues in
218 the periphery and functions cell-non-autonomously for the engulfment of dendrites. Our data
219 also suggest that, compared to the fat body, neurons are a less effective source of Orion for
220 engulfment of dendrites.

221 **Phosphatidylserine exposure is necessary and sufficient for Orion to bind to the cell surface**

To further understand the engulfment defects in *orion* mutants, we examined PS exposure on injured dendrites. We used fat body-derived Annexin V-mCardinal (AV-mCard) as a PS sensor; it labels injured but not healthy dendrites (Sapar et al., 2018). AV-mCard robustly labeled

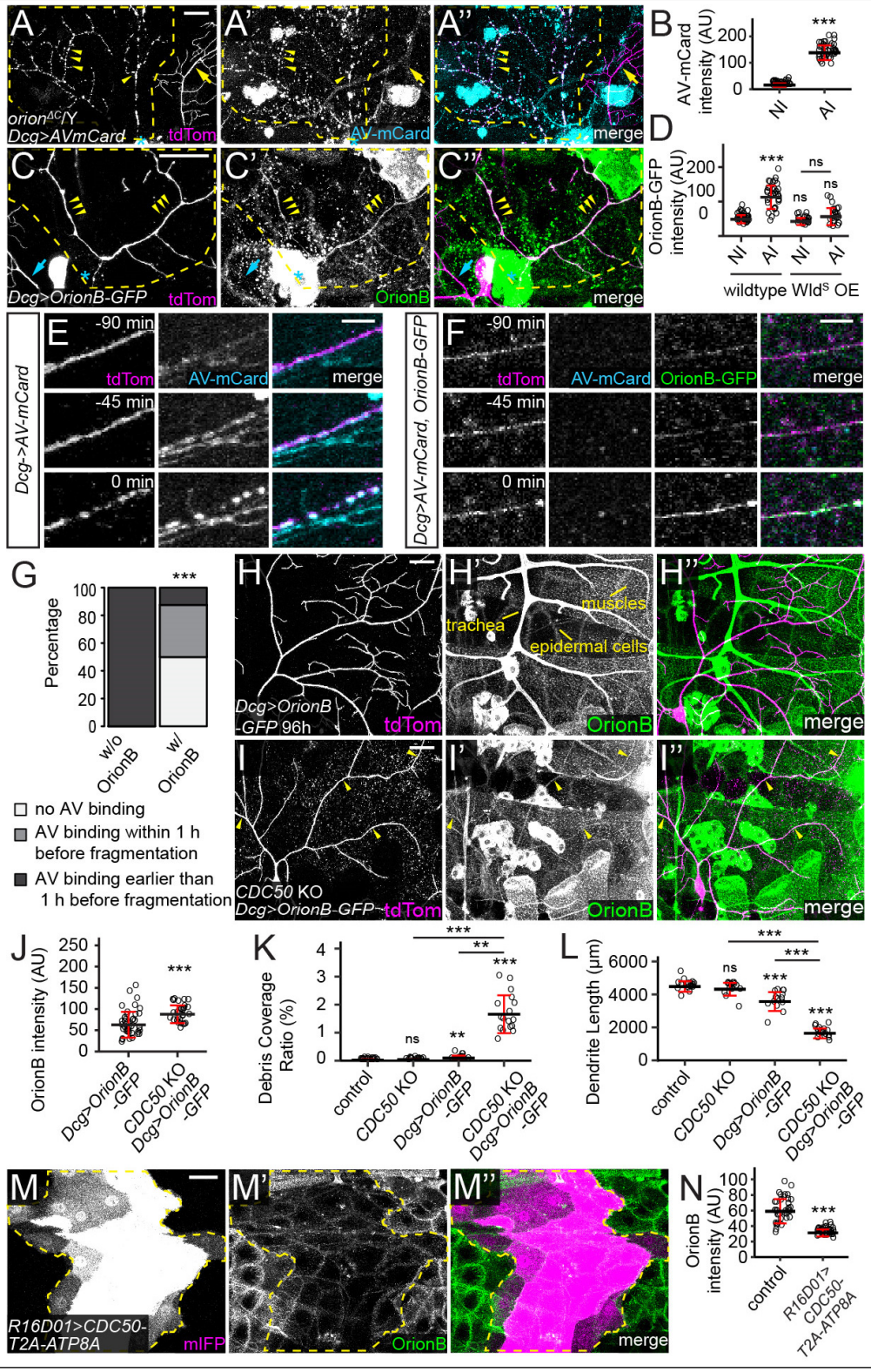

Figure 3: PS exposure is necessary and sufficient for Orion to bind to the cell surface

(A-A") Labeling of injured dendrites of a ddaC neuron by AV-mCard at 23 hrs AI in *orion*$^{\Delta C}$ hemizygous larvae. Yellow arrowheads: injured dendrites with AV-mCard labeling; yellow arrows: uninjured dendrites lacking AV-mCard labeling.

(B) Quantification of AV-mCard binding on dendrites. AV-mCard intensities were measured on both uninjured (NI) and injured (AI) dendrites. n = number of measurements: NI (n = 39, 8 animals); AI (n = 39, 8 animals). Welch's t-test.

Continue in next page.

Figure 3 legend continued.

(C-C") Labeling of injured dendrites of a ddaC neuron by Orion-GFP at 6 hrs AI in wildtype larvae. Yellow arrowheads: injured dendrites with OrionB-GFP labeling.

(D) Quantification of Orion-GFP binding on dendrites of wildtype and Wld^S OE neurons. n = number of measurements: wildtype NI (n = 39, 10 animals); wildtype AI (n = 36, 10 animals); Wld^S OE NI (n = 22, 6 animals); Wld^S OE AI (n = 23, 6 animals). Kruskal-Wallis (One-way ANOVA on ranks) and Dunn's test, p-values adjusted with the Benjamini-Hochberg method.

(E-F) Time series of injured dendrites of ddaC neurons from 90 min before fragmentation to the moment of fragmentation, with only AV-mCard expressed (E) or both OrionB-GFP and AV-mCard co-expressed (F) by the fat body. Time stamps are relative to the frame of dendrite fragmentation.

(G) Percentages of injured dendrites showing no AV binding, AV binding within 1 hr before fragmentation, AV binding earlier than 1 hr before fragmentation. n = number of measurements: w/o OrionB OE (n = 9, 5 animals); w/ OrionB OE (n = 8, 3 animals). Fisher's exact test.

(H-I") Distribution of fat body-derived OrionB-GFP with wildtype (H-H") and *CDC50* KO (I-I") dendrites at 96 hrs AEL. Peripheral tissues showing OrionB-binding are labeled in (H'). Yellow arrowheads indicate OrionB-binding on *CDC50* KO dendrites (I-I").

(J) Quantification of OrionB-GFP binding on wildtype and *CDC50* KO dendrites. n = number of measurements: *Dcg>OrionB-GFP* (n = 41, 7 animals); *CDC50* KO + *Dcg>OrionB-GFP* (n = 29, 6 animals). Welch's t-test.

(K-L) Quantification of debris coverage ratio (K) and dendrite length (L) at 96 hrs AEL. n = number of neurons: control (n = 17, 9 animals); *CDC50* KO (n = 15, 8 animals); *Dcg>OrionB-GFP* (n = 13, 8 animals); *CDC50* KO + *Dcg>OrionB-GFP* (n = 17, 9 animals). For (K), Kruskal-Wallis (One-way ANOVA on ranks) and Dunn's test, p-values adjusted with the Benjamini-Hochberg method; for (L), one-way ANOVA and Tukey's test .

(M-M") OrionB-GFP binding on epidermal cells that expressed *CDC50-T2A-ATP8A*. Yellow dash outlines: *CDC50-T2A-ATP8A* overexpressing region.

(N) Quantification of OrionB-GFP binding on wildtype epidermal cells and *CDC50-T2A-ATP8A* OE epidermal cells. n = number of measurements: control (n = 36, 9 animals); *R16D01>CDC50-T2A-ATP8A* (n = 36, 9 animals). Welch's t-test.

In (A-A") and (C-C"), yellow dash outlines: territories originally covered by injured dendrites; blue asterisks: injury sites. Neurons were labeled by *ppk-MApHS* (A-A" and E-E"), and *ppk-CD4-tdTom* (C-C", F-F" and H-I"). Scale bars, 25 μm (A-A", C-C", H-I"), 5 μm (E-F), and 50 μm (M-M"). For all quantifications, **p≤0.01, ***p≤0.001; n.s., not significant. The significance level above each genotype is for comparison with the control. Black bar, mean; red bar, SD. See also Video 1-3 and Figure 3—figure supplement 1.

225 dendrite fragments in $orion^{\Delta C}$ mutant larvae at 24 hrs AI (Figure 3A-3B), suggesting that *orion*
226 LOF does not interfere with PS exposure on injured dendrites and that Orion likely functions
227 downstream of PS exposure in the phagocytosis pathway.

228 Because Orion is a secreted protein, we asked where Orion is located during engulfment.
229 Similar to AV-mCard, we observed strong enrichment of fat body-derived OrionB-GFP on
230 injured dendrites at 4-6 hrs AI (Figure 3C-3D, and Video 1), a timepoint when injured dendrites
231 expose high levels of PS (Sapar et al., 2018). Wld^S, a transgene that carries NMNAT1 activity,
232 suppresses fragmentation and PS exposure of injured dendrites when overexpressed in neurons
233 (Ji et al., 2022; Sapar et al., 2018). Interestingly, Wld^S OE also efficiently suppressed OrionB-
234 GFP enrichment on injured dendrites (Figure 3—figure supplement 1A-1A", and Figure 3D),
235 indicating that PS exposure may be required for Orion binding.

236 To test directly the possibility that Orion interacts with PS on injured dendrites, we asked
237 whether OrionB can compete with AV-mCard for binding to injured dendrites, given that AV
238 binds to PS directly (Leventis and Grinstein, 2010). Using long-term time-lapse imaging (Ji and
239 Han, 2020), we found that fat body-derived AV-mCard accumulated on injured dendrites at least
240 60 minutes before dendrite fragmentation (9/9 movies) (Figures 3E and 3G, and Video 2).
241 However, when both OrionB-GFP and AV-mCard were co-expressed by the fat body, OrionB-
242 GFP was detected on injured dendrites long before fragmentation (8/8 movies), while AV-mCard
243 did not bind the same injured dendrite in half of the cases (4/8 movies) (Figures 3F and 3G, and
244 Video 3). In most cases where AV-mCard was observed on injured dendrites (3/4 movies), the
245 labeling only appeared right at the time of dendrite fragmentation (Figure 3G), when PS
246 exposure is at its peak (Sapar et al., 2018). These results suggest that Orion can outcompete AV
247 for binding to injured dendrites, most likely by directly interacting with PS on the surface of
248 injured dendrites.

249 To test if neuronal PS exposure is sufficient to induce Orion binding, we ectopically
250 induced dendritic PS exposure by knocking out *CDC50* in neurons (Sapar et al., 2018).
251 Distribution of fat body-derived OrionB-GFP was examined at 96 hrs AEL, a time when *CDC50*
252 KO alone is not yet sufficient to cause membrane loss of dendrites (Figures 3K and 3L). OrionB-
253 GFP showed little binding to wildtype dendrites (Figures 3H-3H", and 3J) but bound robustly to
254 *CDC50* KO dendrites (Figures 3I-3J) at this stage. Interestingly, the presence of OrionB-GFP

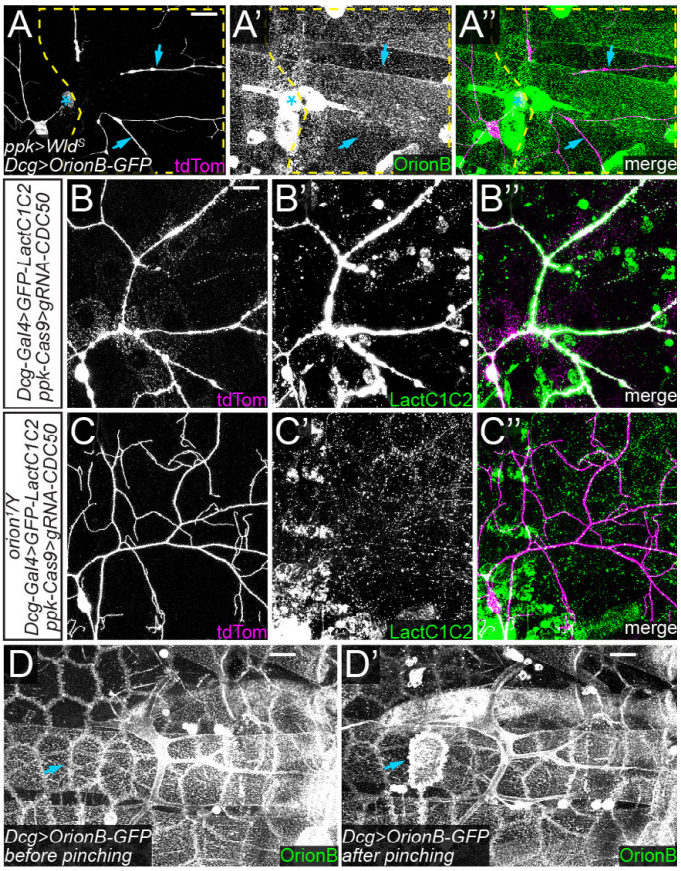

Figure 3—figure supplement 1: PS exposure is necessary and sufficient for Orion to bind to the cell surface

(A-A") Lack of OrionB-GFP labeling on injured dendrites of a ddaC neuron with Wld^S OE at 6 hrs AI. Yellow dash outlines: territories originally covered by injured dendrites; blue asterisks: injury sites; blue arrows: injured dendrites lacking OrionB-GFP labeling.

(B-C") *CDC50* KO neurons in the presence of fat body-derived GFP-LactC1C2 in control (B-B") and *orion*^{1} hemizygous (C-C") larvae.

(D-D') OrionB-GFP binding on epidermal cells before (D) and after (D') gentle pinching. Blue arrows indicate enhanced OrionB binding.

Neurons were labeled by *ppk-CD4-tdTom* (A-C"). In all image panels, scale bars, 25 µm.

255 caused appreciable degeneration of *CDC50* KO dendrites, as indicated by the drastically
256 increased dendrite debris and shortened total dendrite length (Figures 3K and 3L). These results
257 suggest that Orion is recruited to PS-exposing dendrites and OrionB binding on dendrites
258 potentiates epidermal engulfment.

259 The PS-binding C1C2 domain of mouse Lactadherin (LactC1C2) has been used as a PS
260 sensor in multiple systems (Hanayama et al., 2002; Mapes et al., 2012; Sapar et al., 2018;
261 Shacham-Silverberg et al., 2018). We previously reported that fat body-derived LactC1C2 not
262 only labels degenerating dendrites but also promotes degeneration of *CDC50* KO dendrites
263 (Sapar et al., 2018) (Figure 3—figure supplement 1B-1B"). Surprisingly, this degeneration was
264 completely suppressed in the *orion*^{1} hemizygotes (Figure 3—figure supplement 1C-1C"),
265 suggesting that the effects of LactC1C2 are mediated by Orion.

266 We also noticed that OrionB-GFP binds to the surface of several other peripheral tissues,
267 including epidermal cells, muscles, and trachea (Figures 3H-3H"). The OrionB-GFP binding on
268 epidermal cells was enhanced after we gently pinched the larval body wall, which is expected to
269 mildly disrupt the epidermal cell membrane (Figure 3—figure supplement 1D-1D'). We next
270 examined whether these non-neuronal Orion bindings are also mediated by PS. To block PS
271 exposure, we overexpressed ATP8A, an ortholog of the PS-specific flippase TAT-1 (Darland-
272 Ransom et al., 2008; Wehman et al., 2011). Overexpression of ATP8A in da neurons is sufficient
273 to suppress PS exposure and the associated dendrite degeneration caused by *Nmnat* KO (Ji et al.,
274 2022). The P4-ATPase chaperone CDC50 was co-expressed with ATP8A in a patch of epidermal
275 cells to facilitate ATP8A trafficking. Epidermal overexpression of ATP8A and CDC50
276 drastically suppressed OrionB-GFP binding on the surface of epidermal cells (Figures 3M-3N),
277 suggesting that this binding is PS-exposure dependent.

278 Together, our results suggest that PS exposure is both required and sufficient for Orion to
279 bind to the cell surface of both neuronal and non-neural cells.

280 **Orion functions upstream of Drpr**

281 Because *drpr* is the only other gene known to be required for epidermal engulfment of PS-
282 exposing dendrites (Ji et al., 2022; Sapar et al., 2018), we wondered if Orion and Drpr act in the
283 same pathway. We found that *orion*^{1} hemizygous and *drpr* mutant larvae exhibited similar
284 degrees of near complete phagocytosis deficiency in injury-induced dendrite degeneration, as
285 indicated by the portion of unengulfed MApHS-labeled debris (Figures 4A- 4B). Both genotypes
286 also completely rescued *Nmnat* KO-induced dendrite degeneration, as reflected by the debris
287 level and the dendrite length (Figures 4C and 4D). We further asked whether removing both *drpr*
288 and *orion* produces stronger phagocytosis defects than the loss of either. Using CRISPR-TRiM,
289 we induced whole-body KO of *orion* and *drpr* individually and together. Injured dendrites
290 showed indistinguishable levels of near complete blockage of engulfment in all three genotypes
291 at 24 hrs AI (Figures 4E-4G), suggesting that *orion* and *drpr* function in the same genetic
292 pathway.

To elucidate the epistatic relationship between *orion* and *drpr*, we tested whether the Orion-PS interaction depends on Drpr and whether gain-of-function (GOF) of one gene can rescue the LOF of the other. At 4-5 hrs AI, OrionB-GFP bound to injured dendrites in wildtype

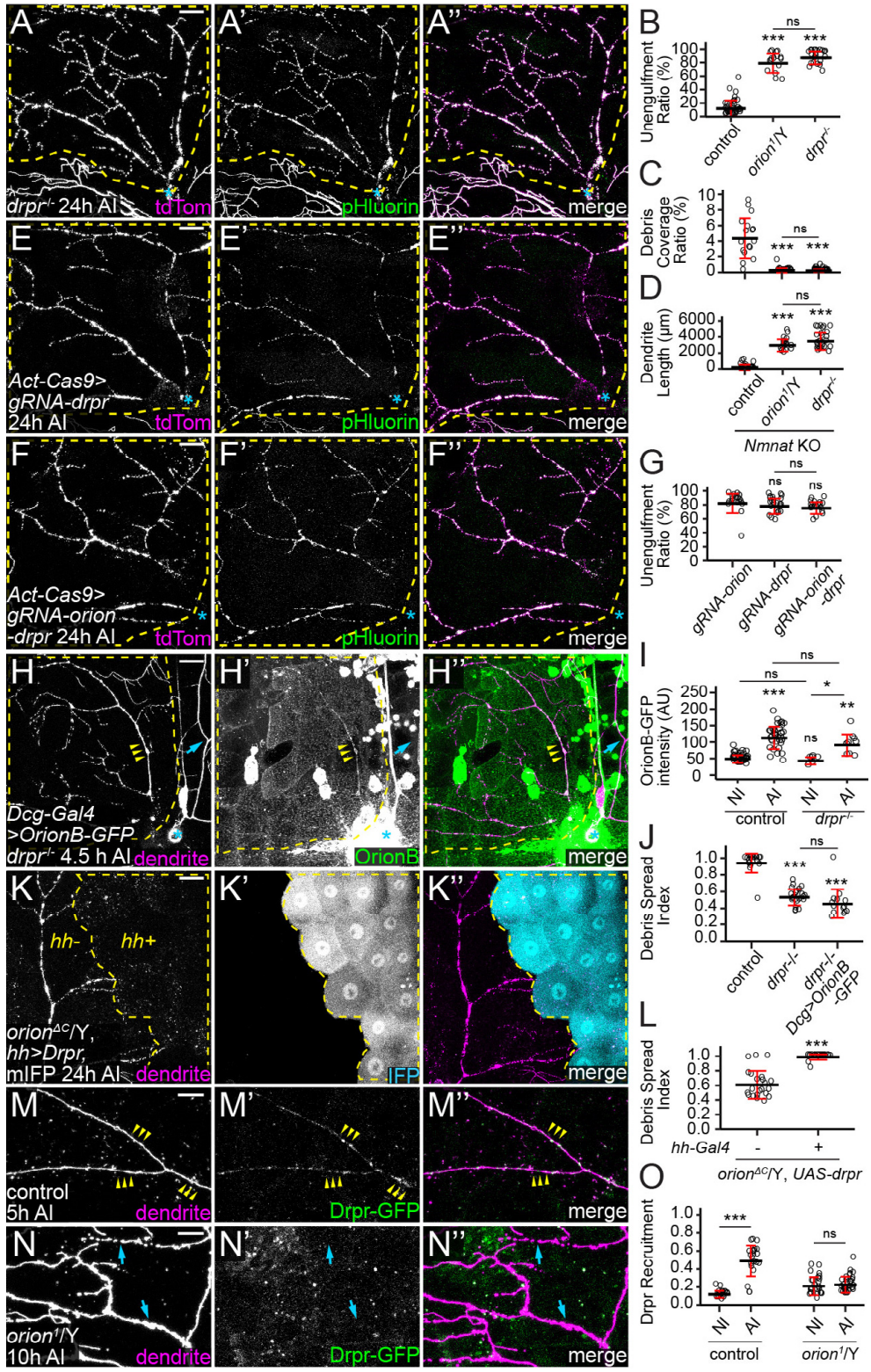

Figure 4: Orion functions upstream of Drpr

(A-A") Partial dendritic fields of a ddaC neuron in *drpr*$^{-/-}$ at 24 hrs AI.

(B) Quantification of unengulfment ratio of injured dendrites. n = number of neurons: control and *orion*^{1}/Y (same dataset as in Figure 1D); *drpr*$^{-/-}$ (n = 23, 10 animals). One-way ANOVA and Tukey's test.

(C-D) Quantification of debris coverage ratio (C) and dendrite length (D) at 120 hrs AEL. n = number of neurons: *Nmnat* KO in wildtype and in *orion*^{1}/*Y* (same dataset as in Figure 1K); *Nmant* KO in *drpr*$^{-/-}$ (n = 28, 14 animals). Kruskal-Wallis (One-way ANOVA on ranks) and Dunn's test, p-values adjusted with the Benjamini-Hochberg method.

Continue in next page.

Figure 4 legend continued.

(E-F") Partial dendritic fields of ddaC neurons at 24 hrs AI with whole-body *drpr* KO (E-E"), and *drpr+orion* double KO (F-F").

(G) Quantification of unengulfment ratio of injured dendrites. n = number of neurons: *orion* KO (same dataset as in Figure 2F); *drpr* KO (n = 23, 12 animals); *orion+drpr* double KO (n = 19, 10 animals). One-way ANOVA and Tukey's test.

(H-H") Labeling of injured dendrites of a ddaC neuron by OrionB-GFP in $drpr^{-/-}$ at 4.5 hrs AI. Yellow arrowheads: injured dendrites with OrionB-GFP labeling; blue arrows: uninjured dendrites lacking OrionB-GFP binding.

(I) Quantification of Orion-GFP binding on dendrites in the wildtype and the $drpr^{-/-}$ larvae. n = number of measurements: wildtype NI and wildtype AI (same dataset as in Figure 3D); $drpr^{-/-}$ NI (n = 6, 2 animals); $drpr^{-/-}$ AI (n = 9, 3 animals). Kruskal-Wallis (One-way ANOVA on ranks) and Dunn's test, p-values adjusted with the Benjamini-Hochberg method.

(J) Quantification of debris spread index of injured dendrites at 22-24 hrs AI. n = number of neurons: control (same dataset as in 2M); $drpr^{-/-}$ (n = 23, 10 animals); $drpr^{-/-}$ + *Dcg>OrionB-GFP* (n = 14, 7 animals). One-way ANOVA and Tukey's test.

(K-K") Engulfment of injured dendrites in an $orion^{\Delta C}$ hemizygous larva with Drpr overexpressed in the *hh* domain. Yellow dash outlines: *hh>Drpr, mIFP* region.

(L) Quantification of debris spread index of injured dendrites at 22-24 hrs AI in region without Drpr OE and region with Drpr OE in $orion^{\Delta C}/Y$. n = number of neurons: region without Drpr OE (n = 22, 12 animals); and region with Drpr OE (n = 24, 12 animals). Welch's t-test.

(M-N") Distribution of Drpr-GFP in the presence of injured dendrites in control at 5 hrs AI (M-M") and in $orion^{1}/Y$ at 10 hrs AI (N-N"). Yellow arrowheads (M-M"): injured dendrites with Drpr-GFP recruitment; bule arrowheads (N-N"): injured dendrites lacking Drpr-GFP recruitment.

(O) Quantification of Drpr-GFP recruitment (Drpr-GFP-positive area on dendrites/total dendrite area). n = measurements: control NI (n = 20, 12 animals); control AI (n = 21, 12 animals); $orion^{1}/Y$ NI (n = 27, 8 animals); $orion^{1}/Y$ AI (n = 31, 8 animals). Welch's t-test.

Neurons were labeled by *ppk-MApHS* (A-A", E-E" and F-F"), and by *ppk-CD4-tdTom* (H-H", K-K", and M-N"). In (A-A"), (E-E"), (F-F") and (H-H"), yellow dash outlines: territories originally covered by injured dendrites; blue asterisks: injury sites. Scale bars, 25 μm (A-A", E-E", F-F", H-H", K-K") and 10 μm (M-N"). For all quantifications, *p≤0.05, **p≤0.01, ***p≤0.001; n.s., not significant. The significance level above each genotype is for comparison with the control. Black bar, mean; red bar, SD. See also Figure 4—figure supplement 1.

and *drpr* null larvae at similar levels (Figure 4H-4I), demonstrating that Orion does not need Drpr for binding to PS. Two observations further suggest that Orion GOF cannot compensate for the loss of *drpr* in engulfment: First, overexpression of Orion in the fat body did not rescue the engulfment of injured dendrites in *drpr* mutants at 24 hrs AI (Figure 4—figure supplement 1A and Figure 4J); and second, the degeneration of *CDC50* KO dendrites induced by OrionB-GFP (Figure 3I-3L) was absent in *drpr* mutants (Figure 4—figure supplement 1B-1D). To test the converse possibility that *drpr* GOF can rescue *orion* LOF, we overexpressed Drpr in a patch of epidermal cells in the posterior hemisegment (driven by *hh-Gal4*) of $orion^{\Delta C}$ hemizygotes. Interestingly, Drpr OE restored engulfment of injured dendrites, as indicated by the dispersion of dendrite debris specifically in the *hh* domain (Figures 4K-4L). These data indicate that Drpr functions downstream of Orion, and that high levels of Drpr can compensate for the loss of Orion in phagocytosis.

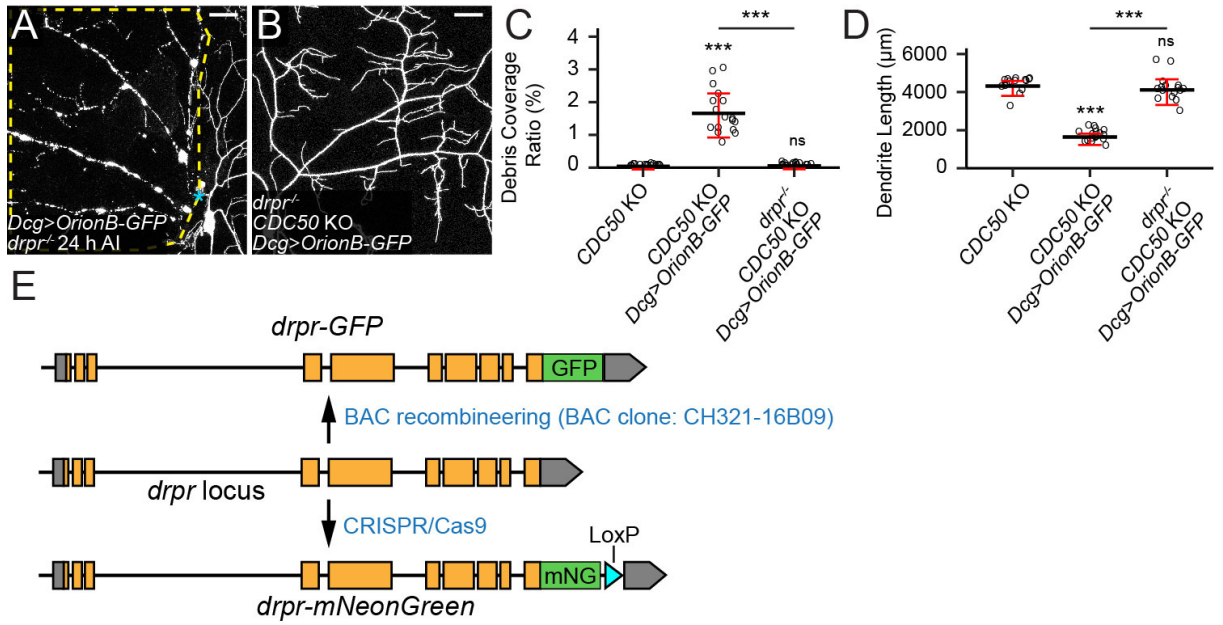

Figure 4—figure supplement 1: Orion functions upstream of Drpr

(A) Partial dendritic fields of an injured ddaC neuron with OrionB-GFP OE in fat body in the *drpr*$^{-/-}$ background at 24 hrs AI.

(B) Partial dendritic fields of a *CDC50* KO neuron with OrionB-GFP OE in fat body in the *drpr*$^{-/-}$ background.

(C-D) Quantification of debris coverage ratio (C) and dendrite length (D). n = number of neurons: *CDC50* KO and *CDC50* KO + *Dcg>OrionB-GFP* (96 hrs AEL, same dataset as in Figure 3K); *drpr*$^{-/-}$ + *CDC50* KO + *Dcg>OrionB-GFP* (120 hrs AEL, n = 16, 8 animals). For (C), Kruskal-Wallis (One-way ANOVA on ranks) and Dunn's test, p-values adjusted with the Benjamini-Hochberg method; for (D), one-way ANOVA and Tukey's test; ***p≤0.001; n.s., not significant. The significance level above each genotype is for comparison with the control. Black bar, mean; red bars, SD.

(E) Schematic representation of Drpr-GFP and Drpr-mNG. Yellow boxes indicate exons, grey boxes indicate untranslated regions.

For both image panels, neurons were labeled by *ppk-CD4-tdTom*. Scale bars, 25 µm.

To further understand how *orion* LOF affects Drpr, we examined the distribution of Drpr protein by live imaging. For this purpose, we generated a knock-in allele of *drpr* so that the C-terminus of endogenous Drpr is tagged by mNeonGreen (mNG) (Shaner et al., 2013) (Figure 4—figure supplement 1E). To further boost the Drpr signal, we also made a Drpr-GFP transgene that contains a genomic fragment of the *drpr* locus tagged with GFP at the Drpr C-terminus (Figure 4—figure supplement 1E). Combining a copy of each of *drpr-mNG* and *drpr-GFP* (referred to as simply *drpr-GFP* because both fluorescent proteins are green), we were able to see robust Drpr recruitment to injured dendrites prior to dendrite fragmentation in the wildtype (Figures 4M-4M" and 4O). However, this recruitment was abolished in the *orion*^{1} hemizygote, even though injured dendrites showed signs of degeneration, such as thinning and blebbing (Figures 4N-4O). These results suggest that Orion regulates Drpr's response to degenerating dendrites after injury.

Orion mediates the interaction between PS and Drpr

Because Orion interacts with PS and functions upstream of Drpr, we wondered whether Orion mediates PS recognition by interacting with Drpr. We first tested whether Orion could bind to Drpr *in vivo* by expressing Drpr in a patch of epidermal cells (driven by *R16D01-Gal4*). Fat body-derived OrionB-GFP was found to accumulate specifically on the surface of these Drpr OE cells in wandering 3rd instar larvae (Figures 5A-5B). Interestingly, some epidermal cells with higher OrionB-GFP enrichment (due to higher Gal4 activities) extruded into neighboring

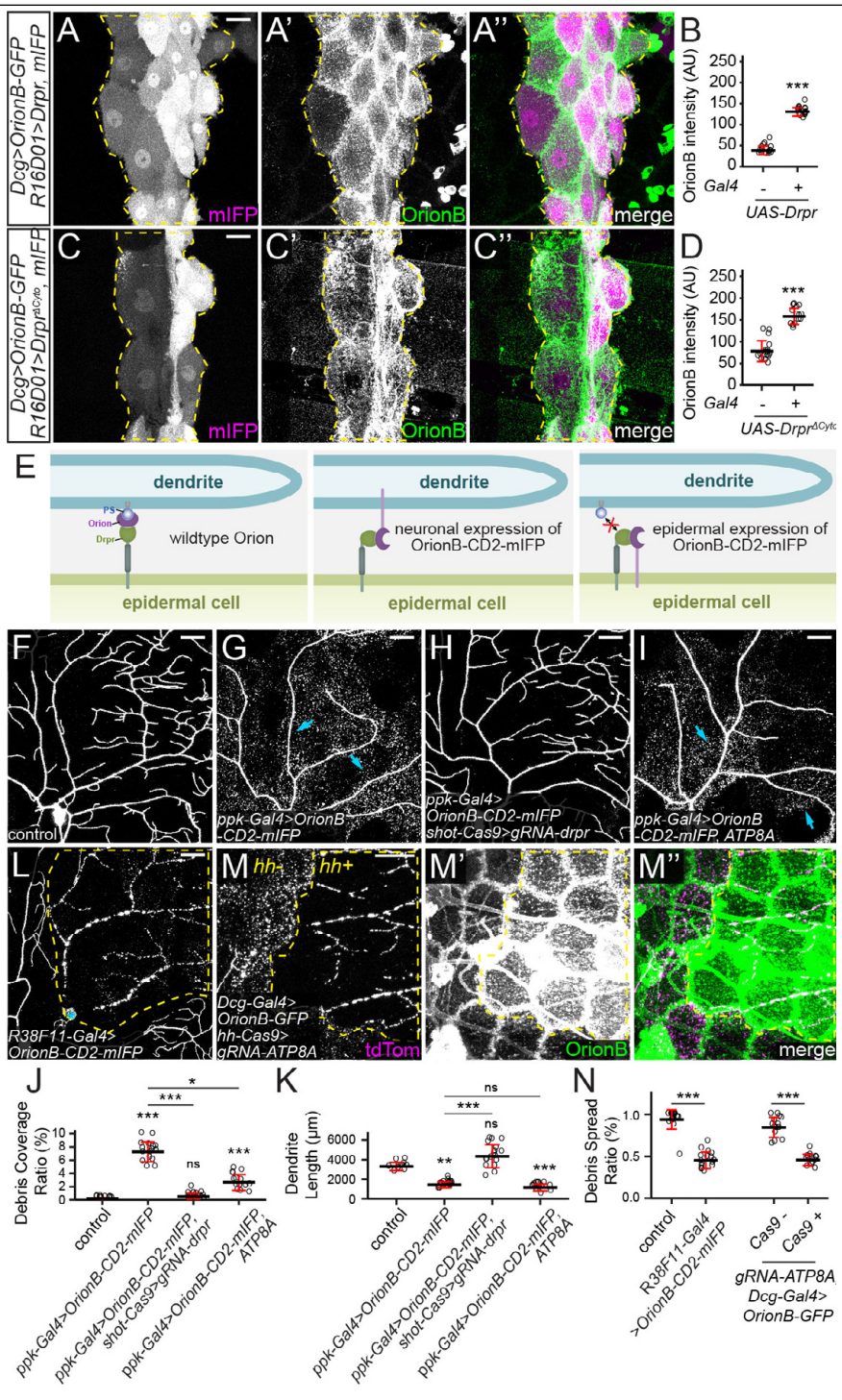

Figure 5: Orion mediates the interaction between PS and Drpr

(A-A") Distribution of fat body-derived OrionB-GFP with Drpr overexpressed in a patch of epidermal cells driven by R16D01-Gal4. mIFP was coexpressed with Drpr and thus the mIFP intensity is correlated with the Gal4 activity. Yellow dash outlines: Drpr OE region.

(B) Quantification of Orion-GFP binding on epidermal cells with or without Drpr OE. n = number of measurements: without Drpr OE (n = 16, 8 animals); with Drpr OE (n = 16, 8 animals). Welch's t-test.

(C) Distribution of fat body-drived OrionB-GFP with Drpr$^{\Delta Cyto}$ overexpressed in a patch of epidermal cells (labeled by mIFP). Yellow dash outlines: Drpr$^{\Delta Cyto}$ OE region.

(D) Quantification of Orion-GFP binding on epidermal cells with or without Drpr$^{\Delta Cyto}$ OE. n = number of measurements: without Drpr$^{\Delta Cyto}$ OE (n = 16, 8 animals); with Drpr$^{\Delta Cyto}$ OE (n = 14, 7 animals). Welch's t-test.

(E) Models of Orion function in mediating PS-Drpr interaction (left), interactions between Drpr and Orion-CD2-mIFP overexpressed by neurons (middle) or epidermal cells (right).

Continue in next page.

Figure 5 legend continued.

(F-I) Partial dendritic fields of a control ddaC neuron (F), an OroinB-CD2-mIFP OE neuron (G), an OroinB-CD2-mIFP OE neuron with *drpr* KO in epidermal cells (H), and an OroinB-CD2-mIFP + ATP8A OE neuron (I).

(J-K) Quantification of debris coverage ratio (J) and dendrite length (K) at 96 hrs AEL. n = number of neurons: control (n = 10, 6 animals); *ppk-Gal4>OroinB-CD2-mIFP* (n = 17, 9 animals); *ppk-Gal4>OroinB-CD2-mIFP + shot-Cas9>gRNA-drpr* (n = 17, 9 animals); *ppk-Gal4>OroinB-CD2*-mIFP, *ATP8A* (n = 14, 7 animals). Kruskal-Wallis (One-way ANOVA on ranks) and Dunn's test, p-values adjusted with the Benjamini-Hochberg method.

(L) Partial dendritic field of an injured ddaC neuron at 25 hrs AI with OroinB-CD2-mIFP expressed in all epidermal cells.

(M-M") Partial dendritic field of an injured ddaC neuron at 9 hrs AI when OroinB-GFP was expressed in fat body and *ATP8A* was knocked out in *hh*-epidermal cells.

(N) Quantification of debris spread index of injured dendrites. n = number of neurons: control (n = 18, 10 animals); *R38F11>OroinB-CD2-mIFP* (n = 16, 8 animals); *Dcg-Gal4>OrionB* (n = 14, 8 animals); *Dcg-Gal4>OrionB + hh-Cas9>ATP8A* (n = 13, 8 animals). Welch's t-test.

Neurons were labeled by *ppk-MApHS* (F-I), and *ppk-CD4-tdTom* (L and M-M"). For all image panels, scale bars, 25 μm. For all quantifications, *p≤0.05, **p≤0.01, ***p≤0.001; n.s., not significant. The significance level above each genotype is for comparison with the control. Black bar, mean; red bar, SD. See also Figure 5—figure supplement 1.

326 epidermal cells that had low or no OrionB-GFP enrichment (Figure 5—figure supplement 1A-
327 1A"). We interpret these extrusions as engulfment of high-OrionB cells by low-OrionB cells. To
328 exclude the possibility that OrionB-GFP was recruited by other cell-surface molecules on
329 epidermal cells as a result of Drpr OE, we also tested a truncated Drpr without the intracellular
330 domain ($Drpr^{\Delta Cyto}$), which should be defective in intracellular signaling. Overexpression of
331 $Drpr^{\Delta Cyto}$ also caused drastic OrionB-GFP accumulation on epidermal cells (Figure 5C-5D).
332 These results suggest that OrionB interacts with the extracellular domain of Drpr directly,
333 perhaps functioning as a bridging molecule between PS and Drpr.

334 To further test this hypothesis, we asked whether expression of an Orion that is
335 permanently tethered to the surface of otherwise wildtype dendrites could bypass the requirement
336 of PS exposure and induce Drpr-dependent phagocytosis. For this purpose, we made an OrionB-
337 CD2-mIFP (mIFP: monomeric infrared fluorescent protein; (Yu et al., 2015)) transgene in which
338 Orion is located on the extracellular side of the CD2 transmembrane domain (Yan et al., 2009).
339 As expected, overexpression of OrionB-CD2-mIFP in neurons caused robust dendrite
340 degeneration (Figures 5E-5G, and 5J-5K). We found that this degeneration was completely
341 suppressed by epidermis-specific KO of *drpr* (Figures 5H, and 5J-5K) but was unaffected by
342 suppressing PS exposure in neurons via ATP8A OE (Figures 5I-5K). These data suggest that
343 membrane-tethered Orion is sufficient to induce PS-independent and Drpr-dependent
344 phagocytosis.

345 Meanwhile, if Orion mediates the recognition of PS by Drpr, we predict that excessive
346 Orion on the surface of epidermal cells would interact with Drpr on the same membrane and
347 interfere with the sensing of PS on dendrites. We first tested this idea by overexpressing OrionB-
348 CD2-mIFP in all epidermal cells (Figure 5E). Indeed, this manipulation fully blocked the
349 engulfment of injured dendrites at 25 hrs AI (Figures 5L and 5N). Drpr was robustly detected on

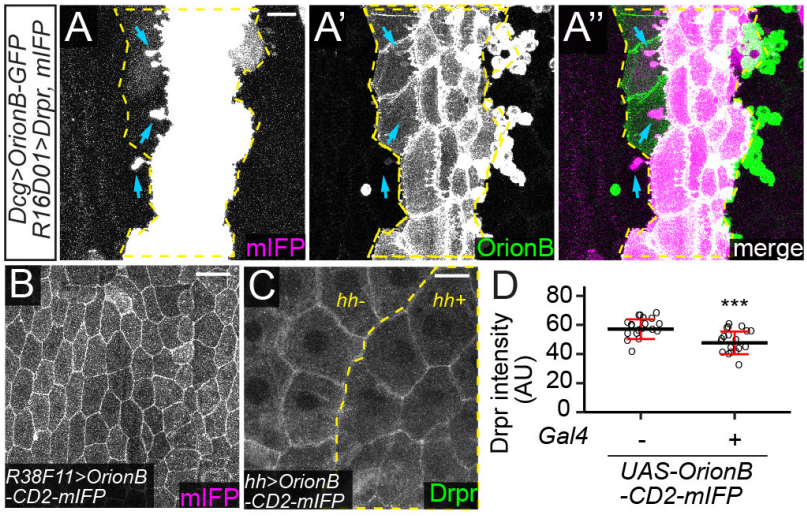

Figure 5—figure supplement 1: Orion mediates the interaction between PS and Drpr

(A-A") Protrusions (blue arrows) extended from Drpr OE epidermal cells (labeled by mIFP) in the presence of fat body-derived OrionB-GFP. Yellow dash outlines: Drpr OE region.

(B) OrionB-CD2-mIFP localization in epidermal cells driven by *R38F11-Gal4*.

(C) Drpr localization in epidermal cells with OrionB-CD2-mIFP expressed in the *hh* domain. Yellow dash outlines: *hh-Gal4>OrionB-CD2-mIFP* region.

(D) Quantification of stained Drpr levels in epidermal cells with or without OrionB-CD2-mIFP OE. n = number of measurements: w/o OrionB-CD2-mIFP OE (n = 19); w/ OrionB-CD2-mIFP OE (n = 19). Welch's t-test; ***$p \leq 0.001$; black bar, mean; red bars, SD.

Scale bars, 25 μm (A-A" and C), 50 μm (B).

the cell membranes of OrionB-CD2-mIFP-expressing cells (Figure 5—figure supplement 1C and 1D), suggesting that the impaired engulfment was not due to defects in Drpr subcellular localization. We then tested whether accumulation of secreted Orion on the surface of epidermal cells has a similar effect in blocking engulfment. Consistent with the idea that Orion binds PS, *ATP8A* KO in epidermal cells resulted in a drastically increased surface level of OrionB-GFP (Figure 5M'). This OrionB-GFP accumulation was associated with phagocytosis deficiency, as indicated by the lack of spread of dendritic debris at 9 hrs AI specifically in the *ATP8A* KO cells (Figure 5M-5N).

Together, our results show that interactions between Orion and Drpr from the same versus apposing membranes produce opposite phenotypes (defective versus dominant dendrite engulfment, respectively) and support the idea that Orion functionally bridges PS and Drpr.

The Orion dosage determines the sensitivity of epidermal cells to PS-exposing dendrites

While examining the phenotypes of the *orion*^{1} mutant, we noticed impaired phagocytosis in *orion*^{1}/+ heterozygous larvae: Neurons with *CDC50* KO and TMEM16F OE showed no signs of membrane loss or degeneration in these animals (Figures 6A, 6I, and 6J), comparable to those in *orion*^{1} hemizygotes. *orion*^{1}/+ larvae also exhibited considerable suppression of *Nmnat* KO-induced dendrite degeneration, albeit not to the level of *orion*^{1} hemizygotes (Figures 6B, 6I, and 6J). However, the engulfment of injured dendrites was normal in *orion*^{1}/+ (Figure 6—figure supplement 1A-1B). Considering that *CDC50* KO and TMEM16F OE causes milder PS exposure than does injury (Sapar et al., 2018), these data suggest that removing half the dosage of Orion reduces the sensitivity of epidermal cells to PS exposure on dendrites but does not block phagocytosis when PS exposure is high. To further test if the Orion dosage determines the ability

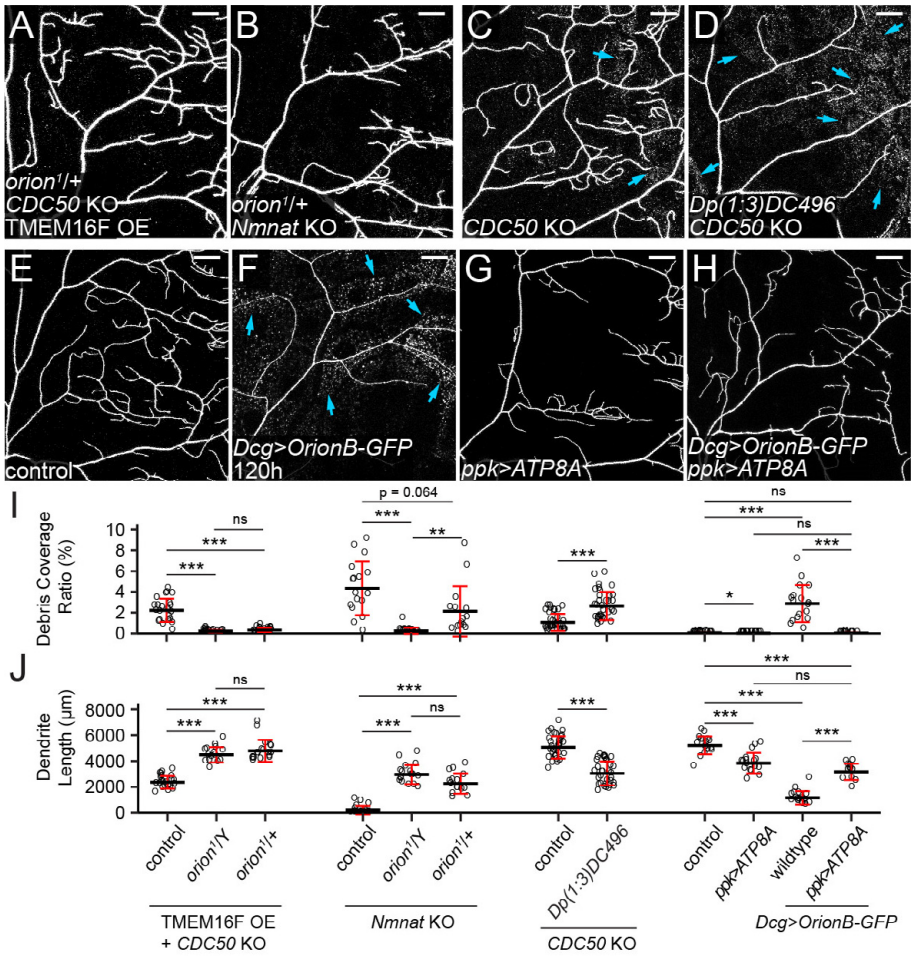

Figure 6: The Orion dosage determines the sensitivity of epidermal cells to PS-exposing dendrites

(A-B) Partial dendritic fields of a TMEM16F OE + *CDC50* KO ddaC neuron (A) and a *Nmnat* KO ddaC neuron (B) in the *orion*[1] heterozygous background.

(C-D) Partial dendritic fields of *CDC50* KO neurons in the control (C) and Dp(1;3)DC496 (D) at 120 hrs AEL. Blue arrows: debris shed from dendrites.

(E-H) Partial dendritic fields of ddaC neurons in the control (E), with fat body-derived OrionB-GFP (F), with ATP8A OE in the neuron (G), and with fat body-derived OrionB-GFP and ATP8A OE in the neuron (H) at 120 hrs AEL.

(I-L) Quantification of debris coverage ratio (I) and dendrite length (L). n = number of neurons: for TMEM16F OE + *CDC50* KO, control and *orion*[1]/Y (same dataset as in Figure 1G), *orion*[1]/+ (n = 18, 9 animals); for (I), Kruskal-Wallis (One-way ANOVA on ranks) and Dunn's test, p-values adjusted with the Benjamini-Hochberg method; for (L), one-way ANOVA and Tukey's test. For *Nmnat* KO, control and *orion*[1]/Y (same dataset as in Figure 1K), *orion*[1]/+ (n = 15, 9 animals); Kruskal-Wallis (One-way ANOVA on ranks) and Dunn's test, p-values adjusted with the Benjamini-Hochberg method. For *CDC50* KO, control (n = 33, 17 animals), Dp(1;3)DC496 (n = 33, 17 animals), Welch's t-test. For effects of *Dcg>OrionB-GFP* and *ppk>ATP8A* at 120 hrs AEL, control (n = 17, 9 animals), *ppk>ATP8A* (n = 17, 9 animals), *Dcg>OrionB-GFP* (n = 17, 9 animals), *ppk>ATP8A + Dcg>OrionB-GFP* (n = 12, 7 animals); for (I), Kruskal-Wallis (One-way ANOVA on ranks) and Dunn's test, p-values adjusted with the Benjamini-Hochberg method; for (L), one-way ANOVA and Tukey's test.

Neurons were labeled by *ppk-MApHS* (A-B and G), *ppk-CD4-tdTom* (C-F), and *ppk-Gal4>CD4-tdTom* (H). For all image panels, scale bars, 25 µm. For all quantifications, *p≤0.05, **p≤0.01, ***p≤0.001; n.s., not significant. The significance level above each genotype is for comparison with the control. Black bar, mean; red bars, SD. See also Figure 6—figure supplement 1.

of epidermal cells to sense PS-exposing dendrites, we increased the Orion dosage by adding an *orion* duplication to the wildtype. The *orion* duplication strongly enhanced the debris level and dendrite loss in a *CDC50* KO background (Figures 6D, 6I, and 6J), which by itself only causes weak PS exposure (Sapar et al., 2018) and low levels of debris (Figures 6D, 6I, and 6J). Thus, extra Orion can indeed increase the sensitivity of epidermal cells to neuronal PS.

377 Further supporting this notion, we found that fat body-derived OrionB bound to wildtype
378 dendrites at 120 hrs AEL (Figure 6—figure supplement 1C) and induced pronounced
379 degeneration (Figures 6E, 6F, and 6I-6J). This degeneration is PS-dependent because it was
380 completely suppressed by ATP8A OE in neurons (Figure 6F-6H, and 6I-6J). This surprising
381 result demonstrates that, in late larval stages, wildtype dendrites expose low levels of PS that
382 cannot be detected by common PS sensors such as AV and LactC1C2, but can be bound by
383 overexpressed Orion.

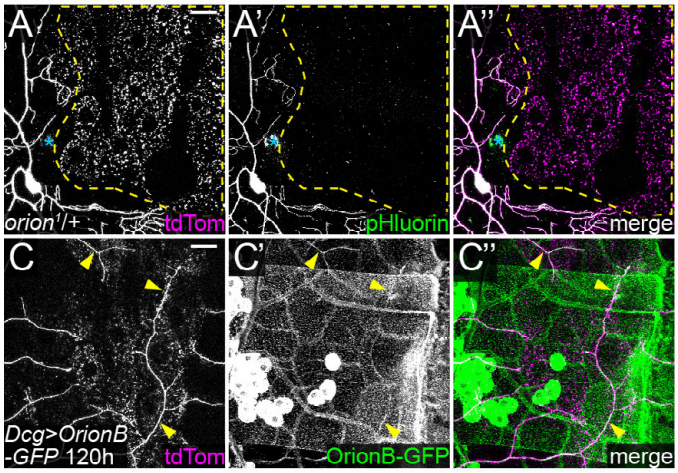

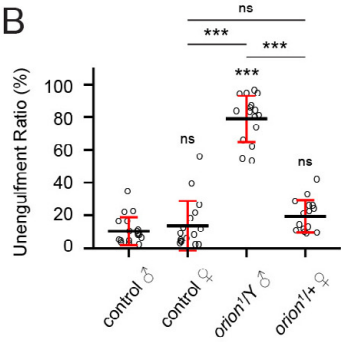

Figure 6—figure supplement 1: The Orion dosage determines the sensitivity of epidermal cells to PS-exposing dendrites

(A-A") Partial dendritic fields of a ddaC neuron in an *orion*^{1} heterozygous larva at 22 hrs AI. Yellow dash outlines: territories originally covered by injured dendrites; blue asterisks: injury sites.

(B) Quantification of unengulfment ratio of injured dendrites. n = number of neurons: control males, control females, and *orion*^{1}/Y (same dataset as in Figure 1D); *orion*^{1}/+ (n = 15, 8 animals). One-way ANOVA and Tukey's test; ***p≤0.001; n.s., not significant. The significance level above each genotype is for comparison with the control. Black bar, mean; red bars, SD.

(C-C") Partial dendritic fields of a wildtype neuron with OrionB-GFP OE in the fat body at 120 hrs AEL. Yellow arrowheads: OrionB-GFP colocalizing with dendrites.

Neurons were labeled by *ppk-MApHS* (A-A"), and *ppk-CD4-tdTom* (C-C"). For all image panels, scale bars, 25 µm.

384 **CX_3C and RRY motifs are important for Orion secretion and binding to PS**

385 Orion shares a CX_3C motif with the human chemokine CX3CL1 and an RRY motif with several
386 human neutrophil peptides. The CX_3C motif is required for Orion's function in MB remodeling
387 (Boulanger et al., 2021), but the importance of the RRY motif in Orion has not been investigated.
388 Structural prediction of OrionB by AlphaFold2 (Jumper et al., 2021) suggests that both motifs
389 are on or near the surface of the protein (Figure 7—figure supplement 1A-1C). To test whether
390 these motifs play any role in PS-mediated dendrite engulfment, we generated *UAS-OrionB-GFP*
391 variants carrying mutations in them (OrionB^{AX3C} and OrionB^{AAY}). In addition, to understand how
392 the G611D point mutation in *orion*^{1} affects Orion function, we also made *UAS-OrionB*^{1}*-GFP*.
393 We first compared these OrionB-GFP variants in their abilities to potentiate dendrite
394 degeneration of *CDC50* KO neurons. Fat body-derived OrionB^{AX3C}, OrionB^{AAY}, and OrionB^{1} all
395 potentiated the debris level of *CDC50* KO neurons (Figures 7A-7D). They also induced various

396 degrees of dendrite reduction as compared to *CDC50* KO alone, with OrionB[1] being the most

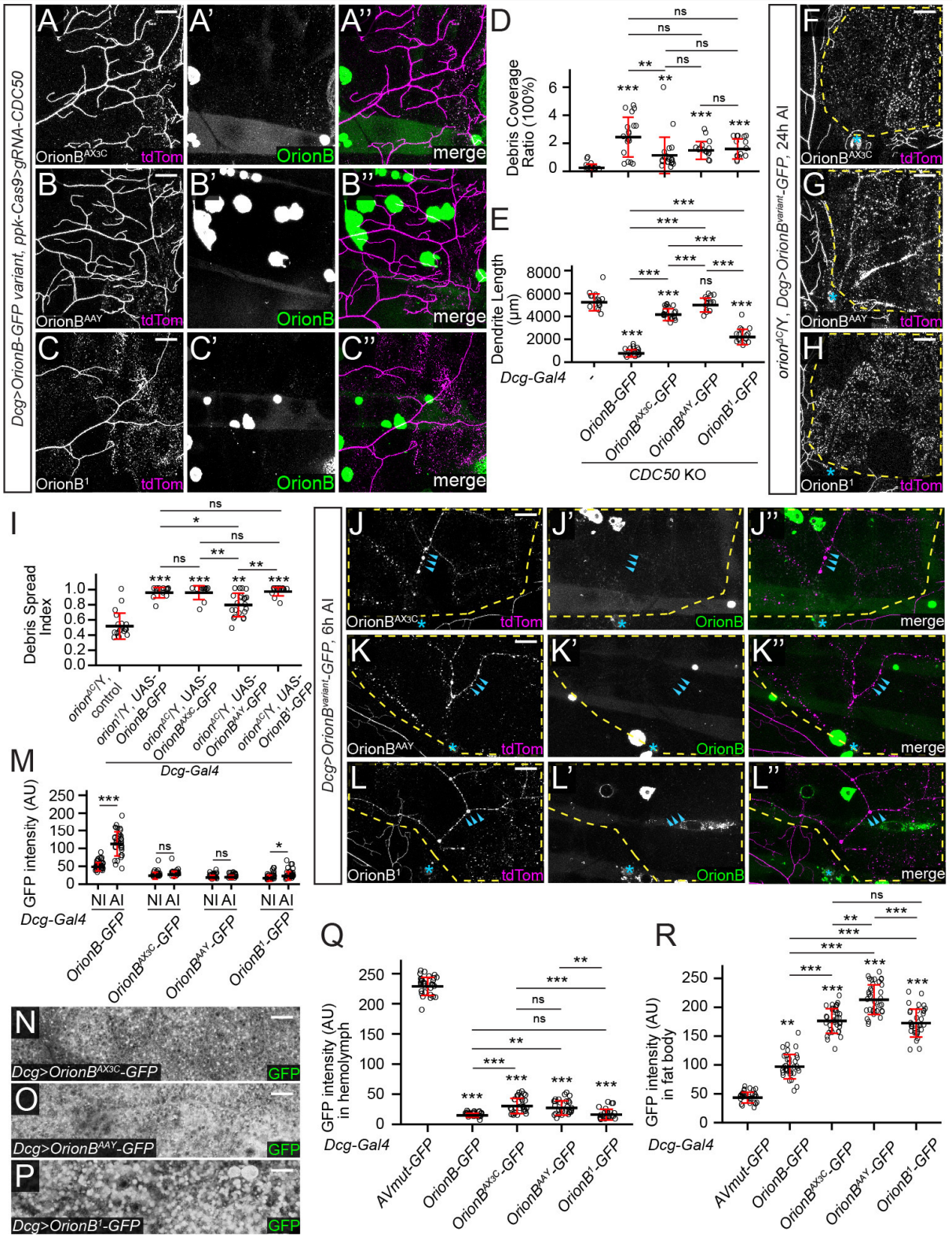

Figure 7: CX$_3$C and RRY motifs are important for Orion secretion and binding to PS

Continue in next page.

Figure 7 legend continued.

(A-C") Partial dendritic fields of *CDC5O* KO ddaC neurons with OrionB^{AX3C}-GFP (A-A"), OrionB^{AAY}-GFP (B-B"), and OrionB^{1}-GFP (C-C") expressed in the fat body at 120 hrs AEL.

(D-E) Quantification of debris coverage ratio (D) and dendrite length (E) at 120 hrs AEL. n = number of neurons: *CDC50* KO control (n = 16, 8 animals); *CDC50* KO + *Dcg>OrionB-GFP* (n = 18, 9 animals); *CDC50* KO + *Dcg>OrionB^{AX3C}-GFP* (n = 20, 10 animals); *CDC50* KO + *Dcg>OrionB^{AAY}-GFP* (n = 16, 8 animals); *CDC50* KO + *Dcg>OrionB^{1}-GFP* (n = 15, 8 animals). For (D), Kruskal-Wallis (One-way ANOVA on ranks) and Dunn's test, p-values adjusted with the Benjamini-Hochberg method; for (E), one-way ANOVA and Tukey's test.

(F) Partial dendritic fields of ddaC neurons in *orion$^{\Delta C}$* hemizygous larvae with OrionB^{AX3C}-GFP (F), OrionB^{AAY}-GFP (G), and OrionB^{1}-GFP (H) expressed by the fat body at 22-24 hrs AI. Yellow dash outlines: territories originally covered by injured dendrites; blue asterisks: injury sites.

(I) Quantification of debris spread index of injured dendrites. n = number of neurons: *orion$^{\Delta C}$*/Y control (n = 19, 9 animals); *orion^{1}*/Y + *Dcg>OrionB-GFP* (same dataset as in 2M); *orion$^{\Delta C}$*/Y + *Dcg>OrionB^{AX3C}-GFP* (n = 12, 7 animals); *orion$^{\Delta C}$*/Y + *Dcg>OrionB^{AAY}-GFP* (n = 23, 12 animals); *orion$^{\Delta C}$*/Y + *Dcg>OrionB^{1}-GFP* (n = 15, 8 animals). Kruskal-Wallis (One-way ANOVA on ranks) and Dunn's test, p-values adjusted with the Benjamini-Hochberg method.

(J-L") OrionB^{variant}-GFP distribution on injured ddaC dendrites with OrionB^{AX3C}-GFP (J-J"), OrionB^{AAY}-GFP (K-K"), and OrionB^{1}-GFP (L-L") expressed by the fat body at 6 hrs AI. Yellow dash outlines: territories originally covered by injured dendrites; blue asterisks: injury sites; blue arrowheads: injured dendrite fragments lacking GFP labeling.

(M) Quantification of GFP binding on injured dendrites. n = number of measurements: *Dcg>OrionB-GFP* NI and AI (same dataset as in 3D); *Dcg>OrionB^{AX3C}-GFP* NI (n = 24, 8 animals); *Dcg>OrionB^{AX3C}-GFP* AI (n = 26, 8 animals); *Dcg>OrionB^{AAY}-GFP* NI (n = 26, 9 animals); *Dcg>OrionB^{AAY}-GFP* AI (n = 27, 9 animals); *Dcg>OrionB^{1}-GFP* NI (n = 36, 9 animals); *Dcg>OrionB^{1}-GFP* AI (n = 36, 9 animals).Welch's t-test.

(N-P) GFP levels in fat bodies expressing OrionB^{AX3C}-GFP (N), OrionB^{AAY}-GFP (O), and OrionB^{1}-GFP (P) at 120 hrs AEL.

(Q) Quantification of GFP levels in hemolymph. AVmut-GFP (Sapar et al., 2018) is a control for maximal secretion. n = number of measurements: *Dcg>AVmut-GFP* (n = 31, 8 animals); *Dcg>OrionB-GFP* (n = 28, 7 animals); *Dcg>OrionB^{AX3C}-GFP* (n = 28, 7 animals); *Dcg>OrionB^{AAY}-GFP* (n = 27, 7 animals); *Dcg>OrionB^{1}-GFP* (n = 22, 7 animals). Kruskal-Wallis (One-way ANOVA on ranks) and Dunn's test, p-values adjusted with the Benjamini-Hochberg method.

(R) Quantification of GFP levels in the fat body. n = number of measurements: *Dcg>AVmut-GFP* (n = 31, 8 animals); *Dcg>OrionB-GFP* (n = 34, 9 animals); *Dcg>OrionB^{AX3C}-GFP* (n = 35, 9 animals); *Dcg>OrionB^{AAY}-GFP* (n = 36, 9 animals); *Dcg>OrionB^{1}-GFP* (n = 34, 9 animals). Kruskal-Wallis (One-way ANOVA on ranks) and Dunn's test, p-values adjusted with the Benjamini-Hochberg method.

Neurons were labeled by *ppk-CD4-tdTom* (A-C", F-H, and J-L"). For all image panels, scale bars, 25 μm. For all quantifications, *p≤0.05, **p≤0.01, ***p≤0.001; n.s., not significant. The significance level above each genotype is for comparison with the control. Black bar, mean; red bars, SD. See also Figure 7—figure supplement 1.

potent and OrionB^{AAY} the least (Figures 7A-7E). However, their effects on dendrite reduction are much weaker (5%-58% reduction) than that of the wildtype OrionB-GFP (85% reduction) (Figures 7D and 7E). We next tested OrionB-GFP variants in rescuing *orion$^{\Delta C}$* hemizygotes with the dendrite injury assay.

All but OrionB^{AAY} restored the engulfment of injured dendrites to the same level as the wildtype OrionB (Figures 7F-7I). These results suggest that these mutations impair, but do not abolish, Orion activity. Among the mutant variants, Orion^{1} seems to have the highest activity whereas OrionB^{AAY} seems to be the least active.

To further determine whether the mutations affect OrionB activity by interfering with its PS-interaction, we examined the binding of OrionB variants on injured dendrites. Whereas WT OrionB-GFP bound to fragmenting dendrites robustly (Figures 3C-3D), none of the mutant variants showed obvious binding (Figures 7J-7M), except that OrionB^{1}-GFP showed occasional colocalization with large pieces of debris. The lack of binding was not due to absence of extracellular OrionB-GFP proteins, as mutant variants showed similar (for OrionB^{1}-GFP) or higher (for OrionB^{AX3C} and OrionB^{AAY}) hemolymph levels as compared to the wildtype OrionB-GFP (Figure 7—figure supplement 1D, 1E, 1F, 1G, and 1Q). These results suggest that the mutant variants have impaired abilities to bind PS on injured dendrites. In addition, distinct from the wildtype OrionB-GFP (Figure 7—figure supplement 1D'), the mutant variants did not show obvious binding on the surface of peripheral tissues (Figure 7—figure supplement 1E', 1F, and 1G').

Lastly, we noticed that all OrionB-GFP mutants were present at higher levels in the fat body than the WT version, with OrionB^{AAY} showing the highest level (Figures 7N-7P, and 7R). Considering that all *UAS-OrionB-GFP* transgenes are identical except for the mutations, and thus should be expressed at comparable levels, these data suggest that these mutations additionally reduce protein secretion from the fat body into the hemolymph.

Together, above results revealed that the CX$_3$C and RRY motifs, as well as G611, are important for the secretion of Orion and for its binding to PS.

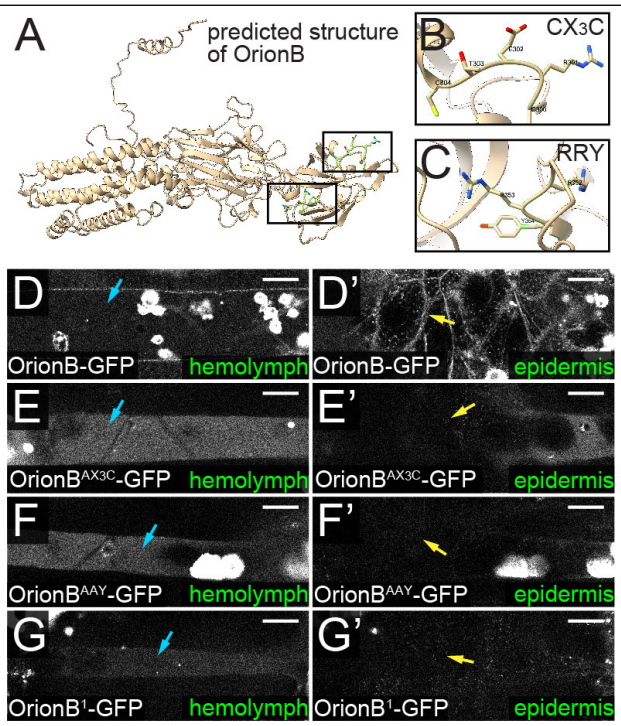

Figure 7—figure supplement 1: CX$_3$C and RRY motifs are important for Orion secretion and binding to PS

(A-C) Structure prediction of OrionB (A, beige) by AlphaFold2. Close-up of putative CX$_3$C (B) and RRY (C) motifs.

(D-G") GFP levels in hemolymph (blue arrowheads) and on epidermal cells (yellow arrowheads) with OrionB-GFP (D and D'), OrionB^{AX3C}-GFP (E and E'), OrionB^{AAY}-GFP (F and F'), and OrionB^{1}-GFP (G and G') expressed by the fat body at 120 hrs AEL. Scale bars, 25 µm.

DISCUSSION

Orion functions as a bridging molecule between PS and Drpr

426 By triggering phagocytosis, the recognition of PS exposed on neurons is a critical event during
427 neurodegeneration and clearance. Although several studies have implied the involvement of Drpr
428 in this process in *Drosophila* (Awasaki et al., 2006; Freeman et al., 2003; Han et al., 2014; Ji et
429 al., 2022; MacDonald et al., 2006; Sapar et al., 2018; Williams et al., 2006), how Drpr mediates
430 PS recognition is unclear. Because the extracellular domain of Drpr can directly interact with PS
431 (Tung et al., 2013), Drpr has been considered as a PS receptor (Williamson and Vale, 2018). In
432 this study, we present several lines of *in vivo* evidence that strongly indicate that the *Drosophila*
433 chemokine-like Orion is a PS-binding bridging molecule that enables Drpr to respond to
434 neuronal PS exposure. First, Orion is required for all scenarios of Drpr-dependent phagocytosis
435 of sensory dendrites and functions upstream of Drpr. Second, Orion binds to PS on the cell
436 surface. We show that Orion binds to neurons and epidermal cells that expose PS as a result of
437 tissue-specific KO of the PS flippase ATP8A. In addition, ATP8A OE, which retains PS in the
438 inner membrane leaflet, eliminates Orion binding on healthy dendrites and epidermal cells,
439 suggesting that this binding is PS-dependent. Importantly, Orion outcompetes Annexin V for
440 binding to injured dendrites, suggesting that Orion directly interacts with PS. Third, when
441 overexpressed, both full-length and intracellular domain-lacking Drpr proteins can trap Orion on
442 the cell surface, suggesting that Drpr interacts with Orion through Drpr's extracellular domain.
443 Lastly, when expressed in neurons, membrane-tethered Orion bypasses the requirement for PS in
444 inducing Drpr-dependent engulfment, but when expressed in phagocytes, membrane-tethered
445 Orion blocks PS-induced engulfment. These observations all point to Orion as a functional link
446 between PS and Drpr.

447 Previously, SIMU, a PS-binding transmembrane protein expressed by *Drosophila*
448 embryonic phagocytes, was originally proposed to be a bridging molecule (Kurant et al., 2008).
449 However, Orion and SIMU contribute to phagocytosis through distinct mechanisms. First, SIMU
450 is expressed by phagocytes to allow them to tether apoptotic cells (Kurant et al., 2008), while
451 Orion is secreted from many peripheral tissues and functions as an opsonin to enable
452 phagocytosis. Second, SIMU is a membrane protein that shares homology with Drpr but
453 functions at a different step in apoptotic neuron clearance compared to Drpr (Kurant et al., 2008).
454 In contrast, as a secreted protein, Orion interacts with Drpr and functions at the same step of
455 phagocytosis as Drpr. Therefore, SIMU behaves more like a tethering receptor (Shklyar et al.,
456 2013), while Orion represents a true PS-bridging molecule in *Drosophila* and is functionally
457 analogous to PS-bridging molecules in other species (Hanayama et al., 2002; Wang et al., 2010).
458 Although we focus our analyses on the engulfment of somatosensory dendrites, the ubiquitous
459 roles of PS and Drpr in phagocytosis and the broad expression patterns of Orion suggest that
460 Orion may be widely involved in PS-mediated phagocytosis in *Drosophila*. This view is
461 supported by our findings that Orion deposited in the hemolymph can mediate phagocytosis in
462 distant tissues and that the accumulation of Orion on epidermal cells turns these cells into targets
463 of phagocytosis.

464 **The level of Orion modulates phagocyte sensitivity to PS**

465 Although the role of PS exposure in inducing phagocytosis has been well documented (Lemke,
466 2019; Nagata, 2018), what determines the sensitivity of phagocytes to PS is much less
467 understood. In this study, we discovered that the available level of secreted PS-bridging
468 molecules is a determinant of phagocyte sensitivity to PS. We show that reducing the dosage of
469 functional Orion by one half makes phagocytes blind to dendrites with moderate levels of PS
470 exposure (i.e. *CDC50* KO + TMEME16F OE neurons and *Nmnat* KO neurons), but the reduced
471 Orion does not affect the ability of phagocytes to engulf dendrites that display high levels of PS
472 exposure (i.e. injury). Conversely, an extra copy of the *orion* locus enhances the ability of
473 phagocytes to engulf dendrites that have mild PS exposure (i.e. *CDC50* KO). These results
474 suggest that endogenous Orion is likely expressed at a balanced level to enable the right amount
475 of phagocytosis: Too much Orion may cause unintended phagocytosis of stressed cells that
476 display mild PS exposure, while too little Orion may interfere with efficient clearance of sick
477 cells or structures that are beyond rescue. Consistent with this idea, endogenous Orion is
478 expressed at a low level during larval development (Figure 2—figure supplement 1F and 1H),
479 but is dramatically upregulated during metamorphosis (Boulanger et al., 2021), a time when
480 large-scale tissue remodeling and clearance take place (Williams and Truman, 2005b).

481 **Orion has distinct roles in neurite maintenance and remodeling**

482 Orion was previously known to be required for axonal pruning and clearance of MB γ neurons
483 during metamorphosis (Boulanger et al., 2021). In that context, Orion is expressed in the
484 remodeling MB neurons and functions as a "find-me" signal for glia to penetrate the axon
485 bundles and engulf axonal debris. In contrast, in the larval peripheral nervous system (PNS),
486 Orion is supplied by many non-neural tissues and functions as a permissive signal for
487 phagocytosis of sick or broken dendrites. This distinction is likely due to two differences
488 between the larval PNS and the remodeling CNS. First, in the PNS, the dendrites of da neurons
489 are exposed to the hemolymph and are readily accessible to Orion that is secreted from other
490 tissues, whereas in the CNS, the axons are more tightly packed and may be harder for extrinsic
491 Orion to access. Neuron-derived Orion would thus be more effective than extrinsic Orion for
492 promoting phagocytosis in the CNS. Intriguingly, we detected Orion expression in a small
493 number of neurons in the larval ventral nerve cord (VNC). It will be interesting to find out
494 whether these neurons are particularly subject to degeneration. Second, compared to the larval
495 PNS where degenerative events are rare, the nervous system undergoing metamorphosis has a
496 much greater demand for phagocytosis. Turning on Orion expression in neurons may thus be
497 required for efficient clearance of all pruned neurites. Consistent with this idea, we detected
498 Orion expression also in a subset of da neurons during metamorphosis.

499 **Orion possesses unique properties compared to other PS-binding molecules**

500 Fluorescent PS probes based on AV and Lact are widely used to visualize PS exposure in cell
501 culture and live animals and have been crucial for many discoveries in PS biology (Andersen et
502 al., 2000; Hanayama et al., 2002; Koopman et al., 1994; Mapes et al., 2012; Sapar et al., 2018).
503 LactC1C2 is known to have a higher affinity to PS than AV (Andree et al., 1990; Shi et al., 2004;

504 Tait and Gibson, 1992). We previously observed additional differences between these two
505 proteins. Compared to LactC1C2, which coats the dendrite surface well, AV tends to traffic to
506 endocytic vesicles inside PS-exposing dendrites, consistent with the ability of the AV complex to
507 induce endocytosis upon PS-binding (Kenis et al., 2004; Oling et al., 2000). Importantly, unlike
508 AV, which does not alter the kinetics of neurite degeneration, LactC1C2 binding to PS-exposing
509 dendrites potentiates Drpr-dependent degeneration (Sapar et al., 2018). This latter observation
510 previously led us to hypothesize that LactC1C2 may contain unknown sequences that interact
511 with Drpr (Sapar et al., 2018). In this study, we show that the effect of LactC1C2 in exacerbating
512 dendrite degeneration depends on Orion, suggesting instead that LactC1C2 may indirectly
513 promote phagocyte/dendrite interactions by enhancing Orion function. One possible mechanism
514 is that LactC1C2 binding on the plasma membrane further disrupts the membrane and causes
515 more PS exposure that can subsequently be detected by endogenous Orion.

516 Compared to AV and LactC1C2, Orion displays unique *in vivo* binding properties.
517 Notably, our evidence suggests that Orion may have the highest affinity for PS among the three.
518 First, it efficiently outcompetes AV in binding to injured dendrites. Second, overexpressed Orion
519 shows PS-dependent binding to healthy epidermal cells and dendrites (albeit the latter only in
520 wandering 3rd instar larvae), while AV and LactC1C2 do not (Sapar et al., 2018). Although we
521 cannot rule out the possibility that Orion also binds other molecules on the cell membrane in a
522 PS-dependent manner, further characterization of the PS-binding domain of Orion may result in
523 novel and exquisitely sensitive PS sensors.

524 The surprising finding that overexpressed Orion binds to peripheral tissues and dendrites
525 suggest that these cells expose PS under physiological conditions, perhaps at a level too low to
526 detect by AV and LactC1C2. Thus, low levels of PS exposure may be much more prevalent *in*
527 *vivo* than previously thought. Intriguingly, binding of overexpressed Orion induces degeneration
528 of wildtype dendrites but does not cause obvious phagocytosis of other non-neural tissues,
529 suggesting that neurons may be more vulnerable to PS-induced phagocytosis than other cell
530 types.

531 **Functional conservation between Orion and human immunomodulatory proteins**

532 Recently, many human chemokines were found to bind to PS exposed on apoptotic vesicles and
533 serve as "find-me" signals to attract phagocytes (Pontejo and Murphy, 2021). Orion shares the
534 CX_3C motif with the mammalian chemokine CXC3L1 and has also three glycosaminoglycan
535 (GAG) putative binding sequences, a hallmark of chemokine activity (Monneau et al., 2016).
536 Even though direct binding to PS has not been demonstrated for CXC3L1, this chemokine is
537 required for microglia-mediated synapse elimination after whisker lesioning (Gunner et al.,
538 2019), a process likely involving PS exposure (Faust et al., 2021). In addition, Orion contains a
539 RRY motif commonly found in human neutrophil peptides, small antimicrobial peptides
540 important for innate immunity (Klotman and Chang, 2006). We found that both CX_3C and RRY
541 motifs are important for Orion function, likely by affecting Orion secretion and PS-binding.
542 Although Orion does not show global sequence homologies to mammalian immunomodulatory

543 proteins, its interaction partner Drpr has mammalian homologs that are involved in phagocytosis
544 of neurons through unknown mechanisms (Wu et al., 2009). Thus, the common features between
545 Orion and human proteins indicate that a functional conservation may exist between PS-sensing
546 mechanisms in insects and humans.

547 **METHODS**

548 **Fly strains**

549 The details of fly strains used in this study are listed in Table S1 (Key Resource Table). For
550 labeling of C4da neurons, we used *ppk-MApHS*, *ppk-CD4-tdTom*, and *ppk-Gal4 UAS-CD4-*
551 *tdTom*. For labeling of all da neurons, we used *21-7-Gal4 UAS-CD4-tdTom*. For labeling PS
552 exposure on dendrites, we used *dcg-Gal4 UAS-AnnexinV-mCard* and *dcg-Gal4 UAS-GFP-*
553 *LactC1C2*. For visualizing OrionB labeling on cell surface, we used *dcg-Gal4 UAS-OrionB-*
554 *GFP*, *Dcg-LexA LexAop-OrionB-GFP*, and *R16A03-LexA LexAop-OrionB-GFP*. We generated
555 *dcg-LexA* by converting the Gal4 in *dcg-Gal4* into LexAGAD. The conversion process will be
556 published elsewhere.

557 See Supplemental Methods for details of molecular cloning and transgenic flies,
558 generation of KI flies, CRISPR-TRiM, live imaging, immunohistochemistry, image analysis and
559 quantification, and statistical analysis. See Table S2 for gRNA target sequences.

560 **ACKNOWLEDGMENTS**

561 We thank Larry Zipursky, Loren Looger, Xinhua Lin, BACPAC Resources Center, *Drosophila*
562 Genomics Resource Center (DGRC), the National Cancer Institute (NCI), and Addgene for
563 plasmids; Marc Freeman and Bloomington Stock Center for fly stocks; Cornell BRC Imaging
564 facility for access to microscopes (funded by NIH grant S10OD018516); Cornell CSCU for
565 advice on statistics; Mike Goldberg for critical reading and suggestions on the manuscript. This
566 work was supported by NIH grants (R01NS099125 and R21OD023824) awarded to C.H., and by
567 ARC grant (PJA 20151203422) and FRM grant (DEQ20160334870) awarded to J.-M.D.

568 **DECLARATION OF INTEREST**

569 The authors declare no competing interests.

570 **REFERENCE**

571 Andersen, M.H., Graversen, H., Fedosov, S.N., Petersen, T.E., and Rasmussen, J.T. (2000).
572 Functional analyses of two cellular binding domains of bovine lactadherin. Biochemistry *39*,
573 6200-6206.
574 Andree, H.A., Reutelingsperger, C.P., Hauptmann, R., Hemker, H.C., Hermens, W.T., and
575 Willems, G.M. (1990). Binding of vascular anticoagulant alpha (VAC alpha) to planar
576 phospholipid bilayers. J Biol Chem *265*, 4923-4928.
577 Awasaki, T., Tatsumi, R., Takahashi, K., Arai, K., Nakanishi, Y., Ueda, R., and Ito, K. (2006).
578 Essential role of the apoptotic cell engulfment genes draper and ced-6 in programmed axon
579 pruning during Drosophila metamorphosis. Neuron *50*, 855-867.
580 Bazan, J.F., Bacon, K.B., Hardiman, G., Wang, W., Soo, K., Rossi, D., Greaves, D.R., Zlotnik, A.,
581 and Schall, T.J. (1997). A new class of membrane-bound chemokine with a CX3C motif. Nature
582 *385*, 640-644.
583 Botelho, R.J., and Grinstein, S. (2011). Phagocytosis. Curr Biol *21*, R533-538.
584 Boulanger, A., Thinat, C., Zuchner, S., Fradkin, L.G., Lortat-Jacob, H., and Dura, J.M. (2021).
585 Axonal chemokine-like Orion induces astrocyte infiltration and engulfment during mushroom
586 body neuronal remodeling. Nat Commun *12*, 1849.
587 Chen, Y., Akin, O., Nern, A., Tsui, C.Y., Pecot, M.Y., and Zipursky, S.L. (2014). Cell-type-specific
588 labeling of synapses in vivo through synaptic tagging with recombination. Neuron *81*, 280-293.
589 Darland-Ransom, M., Wang, X., Sun, C.L., Mapes, J., Gengyo-Ando, K., Mitani, S., and Xue, D.
590 (2008). Role of C. elegans TAT-1 protein in maintaining plasma membrane phosphatidylserine
591 asymmetry. Science *320*, 528-531.
592 Faust, T.E., Gunner, G., and Schafer, D.P. (2021). Mechanisms governing activity-dependent
593 synaptic pruning in the developing mammalian CNS. Nat Rev Neurosci *22*, 657-673.
594 Feng, S., Sekine, S., Pessino, V., Li, H., Leonetti, M.D., and Huang, B. (2017). Improved split
595 fluorescent proteins for endogenous protein labeling. Nat Commun *8*, 370.
596 Freeman, M.R., Delrow, J., Kim, J., Johnson, E., and Doe, C.Q. (2003). Unwrapping glial biology:
597 Gcm target genes regulating glial development, diversification, and function. Neuron *38*, 567-
598 580.
599 Frost, J.L., and Schafer, D.P. (2016). Microglia: Architects of the Developing Nervous System.
600 Trends Cell Biol *26*, 587-597.
601 Fuentes-Medel, Y., Logan, M.A., Ashley, J., Ataman, B., Budnik, V., and Freeman, M.R. (2009).
602 Glia and muscle sculpt neuromuscular arbors by engulfing destabilized synaptic boutons and
603 shed presynaptic debris. PLoS Biol *7*, e1000184.
604 Galloway, D.A., Phillips, A.E.M., Owen, D.R.J., and Moore, C.S. (2019). Phagocytosis in the Brain:
605 Homeostasis and Disease. Front Immunol *10*, 790.
606 Gunner, G., Cheadle, L., Johnson, K.M., Ayata, P., Badimon, A., Mondo, E., Nagy, M.A., Liu, L.,
607 Bemiller, S.M., Kim, K.W.*, et al.* (2019). Sensory lesioning induces microglial synapse elimination
608 via ADAM10 and fractalkine signaling. Nat Neurosci *22*, 1075-1088.
609 Han, C., Song, Y., Xiao, H., Wang, D., Franc, N.C., Jan, L.Y., and Jan, Y.N. (2014). Epidermal cells
610 are the primary phagocytes in the fragmentation and clearance of degenerating dendrites in
611 Drosophila. Neuron *81*, 544-560.

612 Han, C., Wang, D., Soba, P., Zhu, S., Lin, X., Jan, L.Y., and Jan, Y.N. (2012). Integrins regulate
613 repulsion-mediated dendritic patterning of drosophila sensory neurons by restricting dendrites
614 in a 2D space. Neuron *73*, 64-78.
615 Hanayama, R., Tanaka, M., Miwa, K., Shinohara, A., Iwamatsu, A., and Nagata, S. (2002).
616 Identification of a factor that links apoptotic cells to phagocytes. Nature *417*, 182-187.
617 Ji, H., and Han, C. (2020). LarvaSPA, A Method for Mounting Drosophila Larva for Long-Term
618 Time-Lapse Imaging. J Vis Exp.
619 Ji, H., Sapar, M.L., Sarkar, A., Wang, B., and Han, C. (2022). Phagocytosis and self-destruction
620 break down dendrites of Drosophila sensory neurons at distinct steps of Wallerian
621 degeneration. Proceedings of the National Academy of Sciences *119*, e2111818119.
622 Jumper, J., Evans, R., Pritzel, A., Green, T., Figurnov, M., Ronneberger, O., Tunyasuvunakool, K.,
623 Bates, R., Zidek, A., Potapenko, A.*, et al.* (2021). Highly accurate protein structure prediction
624 with AlphaFold. Nature *596*, 583-589.
625 Kenis, H., van Genderen, H., Bennaghmouch, A., Rinia, H.A., Frederik, P., Narula, J., Hofstra, L.,
626 and Reutelingsperger, C.P. (2004). Cell surface-expressed phosphatidylserine and annexin A5
627 open a novel portal of cell entry. J Biol Chem *279*, 52623-52629.
628 Klotman, M.E., and Chang, T.L. (2006). Defensins in innate antiviral immunity. Nat Rev Immunol
629 *6*, 447-456.
630 Koopman, G., Reutelingsperger, C.P., Kuijten, G.A., Keehnen, R.M., Pals, S.T., and van Oers, M.H.
631 (1994). Annexin V for flow cytometric detection of phosphatidylserine expression on B cells
632 undergoing apoptosis. Blood *84*, 1415-1420.
633 Kurant, E., Axelrod, S., Leaman, D., and Gaul, U. (2008). Six-microns-under acts upstream of
634 Draper in the glial phagocytosis of apoptotic neurons. Cell *133*, 498-509.
635 Lemke, G. (2019). How macrophages deal with death. Nat Rev Immunol *19*, 539-549.
636 Leventis, P.A., and Grinstein, S. (2010). The distribution and function of phosphatidylserine in
637 cellular membranes. Annu Rev Biophys *39*, 407-427.
638 Li, T., Chiou, B., Gilman, C.K., Luo, R., Koshi, T., Yu, D., Oak, H.C., Giera, S., Johnson-Venkatesh,
639 E., Muthukumar, A.K.*, et al.* (2020). A splicing isoform of GPR56 mediates microglial synaptic
640 refinement via phosphatidylserine binding. EMBO J *39*, e104136.
641 MacDonald, J.M., Beach, M.G., Porpiglia, E., Sheehan, A.E., Watts, R.J., and Freeman, M.R.
642 (2006). The Drosophila cell corpse engulfment receptor Draper mediates glial clearance of
643 severed axons. Neuron *50*, 869-881.
644 Maciejewski-Lenoir, D., Chen, S., Feng, L., Maki, R., and Bacon, K.B. (1999). Characterization of
645 fractalkine in rat brain cells: migratory and activation signals for CX3CR-1-expressing microglia. J
646 Immunol *163*, 1628-1635.
647 Mapes, J., Chen, Y.Z., Kim, A., Mitani, S., Kang, B.H., and Xue, D. (2012). CED-1, CED-7, and TTR-
648 52 regulate surface phosphatidylserine expression on apoptotic and phagocytic cells. Curr Biol
649 *22*, 1267-1275.
650 Monneau, Y., Arenzana-Seisdedos, F., and Lortat-Jacob, H. (2016). The sweet spot: how GAGs
651 help chemokines guide migrating cells. J Leukoc Biol *99*, 935-953.
652 Nagata, S. (2018). Apoptosis and Clearance of Apoptotic Cells. Annu Rev Immunol *36*, 489-517.
653 Nagata, S., Suzuki, J., Segawa, K., and Fujii, T. (2016). Exposure of phosphatidylserine on the cell
654 surface. Cell Death Differ *23*, 952-961.

655 Oling, F., Santos, J.S., Govorukhina, N., Mazeres-Dubut, C., Bergsma-Schutter, W., Oostergetel,
656 G., Keegstra, W., Lambert, O., Lewit-Bentley, A., and Brisson, A. (2000). Structure of membrane-
657 bound annexin A5 trimers: a hybrid cryo-EM - X-ray crystallography study. J Mol Biol *304*, 561-
658 573.
659 Park, J., Choi, Y., Jung, E., Lee, S.H., Sohn, J.W., and Chung, W.S. (2021). Microglial MERTK
660 eliminates phosphatidylserine-displaying inhibitory post-synapses. EMBO J *40*, e107121.
661 Poe, A.R., Wang, B., Sapar, M.L., Ji, H., Li, K., Onabajo, T., Fazliyeva, R., Gibbs, M., Qiu, Y., Hu, Y.*,*
662 *et al.* (2019). Robust CRISPR/Cas9-Mediated Tissue-Specific Mutagenesis Reveals Gene
663 Redundancy and Perdurance in Drosophila. Genetics *211*, 459-472.
664 Pontejo, S.M., and Murphy, P.M. (2021). Chemokines act as phosphatidylserine-bound "find-
665 me" signals in apoptotic cell clearance. PLoS Biol *19*, e3001259.
666 Port, F., Chen, H.M., Lee, T., and Bullock, S.L. (2014). Optimized CRISPR/Cas tools for efficient
667 germline and somatic genome engineering in Drosophila. Proc Natl Acad Sci U S A *111*, E2967-
668 2976.
669 Salter, M.W., and Stevens, B. (2017). Microglia emerge as central players in brain disease. Nat
670 Med *23*, 1018-1027.
671 Sapar, M.L., Ji, H., Wang, B., Poe, A.R., Dubey, K., Ren, X., Ni, J.Q., and Han, C. (2018).
672 Phosphatidylserine Externalization Results from and Causes Neurite Degeneration in
673 Drosophila. Cell Rep *24*, 2273-2286.
674 Scott-Hewitt, N., Perrucci, F., Morini, R., Erreni, M., Mahoney, M., Witkowska, A., Carey, A.,
675 Faggiani, E., Schuetz, L.T., Mason, S.*, et al.* (2020). Local externalization of phosphatidylserine
676 mediates developmental synaptic pruning by microglia. EMBO J *39*, e105380.
677 Segawa, K., and Nagata, S. (2015). An Apoptotic 'Eat Me' Signal: Phosphatidylserine Exposure.
678 Trends Cell Biol *25*, 639-650.
679 Shacham-Silverberg, V., Sar Shalom, H., Goldner, R., Golan-Vaishenker, Y., Gurwicz, N.,
680 Gokhman, I., and Yaron, A. (2018). Phosphatidylserine is a marker for axonal debris engulfment
681 but its exposure can be decoupled from degeneration. Cell Death Dis *9*, 1116.
682 Shaner, N.C., Lambert, G.G., Chammas, A., Ni, Y., Cranfill, P.J., Baird, M.A., Sell, B.R., Allen, J.R.,
683 Day, R.N., Israelsson, M.*, et al.* (2013). A bright monomeric green fluorescent protein derived
684 from Branchiostoma lanceolatum. Nat Methods *10*, 407-409.
685 Shi, J., Heegaard, C.W., Rasmussen, J.T., and Gilbert, G.E. (2004). Lactadherin binds selectively
686 to membranes containing phosphatidyl-L-serine and increased curvature. Biochim Biophys Acta
687 *1667*, 82-90.
688 Shklyar, B., Levy-Adam, F., Mishnaevski, K., and Kurant, E. (2013). Caspase activity is required
689 for engulfment of apoptotic cells. Mol Cell Biol *33*, 3191-3201.
690 Sievers, C., Platt, N., Perry, V.H., Coleman, M.P., and Conforti, L. (2003). Neurites undergoing
691 Wallerian degeneration show an apoptotic-like process with Annexin V positive staining and
692 loss of mitochondrial membrane potential. Neurosci Res *46*, 161-169.
693 Suzuki, J., Umeda, M., Sims, P.J., and Nagata, S. (2010). Calcium-dependent phospholipid
694 scrambling by TMEM16F. Nature *468*, 834-838.
695 Szymczak, A.L., Workman, C.J., Wang, Y., Vignali, K.M., Dilioglou, S., Vanin, E.F., and Vignali, D.A.
696 (2004). Correction of multi-gene deficiency in vivo using a single 'self-cleaving' 2A peptide-
697 based retroviral vector. Nat Biotechnol *22*, 589-594.

698 Tait, J.F., and Gibson, D. (1992). Phospholipid binding of annexin V: effects of calcium and
699 membrane phosphatidylserine content. Arch Biochem Biophys *298*, 187-191.
700 Tao, J., and Rolls, M.M. (2011). Dendrites have a rapid program of injury-induced degeneration
701 that is molecularly distinct from developmental pruning. J Neurosci *31*, 5398-5405.
702 Tung, T.T., Nagaosa, K., Fujita, Y., Kita, A., Mori, H., Okada, R., Nonaka, S., and Nakanishi, Y.
703 (2013). Phosphatidylserine recognition and induction of apoptotic cell clearance by Drosophila
704 engulfment receptor Draper. J Biochem *153*, 483-491.
705 Wang, X., Li, W., Zhao, D., Liu, B., Shi, Y., Chen, B., Yang, H., Guo, P., Geng, X., Shang, Z*., et al.*
706 (2010). Caenorhabditis elegans transthyretin-like protein TTR-52 mediates recognition of
707 apoptotic cells by the CED-1 phagocyte receptor. Nat Cell Biol *12*, 655-664.
708 Wehman, A.M., Poggioli, C., Schweinsberg, P., Grant, B.D., and Nance, J. (2011). The P4-ATPase
709 TAT-5 inhibits the budding of extracellular vesicles in C. elegans embryos. Curr Biol *21*, 1951-
710 1959.
711 Williams, D.W., Kondo, S., Krzyzanowska, A., Hiromi, Y., and Truman, J.W. (2006). Local caspase
712 activity directs engulfment of dendrites during pruning. Nat Neurosci *9*, 1234-1236.
713 Williams, D.W., and Truman, J.W. (2005a). Cellular mechanisms of dendrite pruning in
714 Drosophila: insights from in vivo time-lapse of remodeling dendritic arborizing sensory neurons.
715 Development *132*, 3631-3642.
716 Williams, D.W., and Truman, J.W. (2005b). Remodeling dendrites during insect metamorphosis.
717 J Neurobiol *64*, 24-33.
718 Williamson, A.P., and Vale, R.D. (2018). Spatial control of Draper receptor signaling initiates
719 apoptotic cell engulfment. J Cell Biol *217*, 3977-3992.
720 Wu, H.H., Bellmunt, E., Scheib, J.L., Venegas, V., Burkert, C., Reichardt, L.F., Zhou, Z., Farinas, I.,
721 and Carter, B.D. (2009). Glial precursors clear sensory neuron corpses during development via
722 Jedi-1, an engulfment receptor. Nat Neurosci *12*, 1534-1541.
723 Yan, D., Wu, Y., Feng, Y., Lin, S.C., and Lin, X. (2009). The core protein of glypican Dally-like
724 determines its biphasic activity in wingless morphogen signaling. Dev Cell *17*, 470-481.
725 Yu, D., Baird, M.A., Allen, J.R., Howe, E.S., Klassen, M.P., Reade, A., Makhijani, K., Song, Y., Liu,
726 S., Murthy, Z*., et al.* (2015). A naturally monomeric infrared fluorescent protein for protein
727 labeling in vivo. Nat Methods *12*, 763-765.
728 Zhai, R.G., Rizzi, M., and Garavaglia, S. (2009). Nicotinamide/nicotinic acid mononucleotide
729 adenylyltransferase, new insights into an ancient enzyme. Cell Mol Life Sci *66*, 2805-2818.
730 Zhou, Z., Hartwieg, E., and Horvitz, H.R. (2001). CED-1 is a transmembrane receptor that
731 mediates cell corpse engulfment in C. elegans. Cell *104*, 43-56.
732 Zhu, X., Libby, R.T., de Vries, W.N., Smith, R.S., Wright, D.L., Bronson, R.T., Seburn, K.L., and
733 John, S.W. (2012). Mutations in a P-type ATPase gene cause axonal degeneration. PLoS Genet *8*,
734 e1002853.
735

736 **VIDEO LEGENDS**

737 **Video 1**: OrionB-GFP labels degenerating dendrites after injury, related to Figure 3. Time-lapse
738 movie of laser-injured ddaC dendrites from 2.5 to 11 hrs AI, showing OrionB-GFP labeling on
739 injured dendrites. The dendrite arbor on the bottom right was injured while the ones at the top
740 were not. The mobile cells in the OrionB-GFP channel are hemocytes. Time stamp is relative to
741 the first frame.

742 **Video 2**: AV-mCard labels injured dendrites before dendrite fragmentation, related to
743 Figure 3. Time-lapse movie of laser-injured ddaC dendrites from 2.5 to 5 hrs AI, showing AV-
744 mCard labeling on injured dendrites as early as 2 hrs before fragmentation. The AV-mCard
745 signals that do not colocalize with tdTom signals indicate AV-mCard labeling on injured
746 dendrites of other types of neurons. Time stamp is relative to the frame of dendrite
747 fragmentation.

748 **Video 3**: AV-mCard fails to label injured dendrites when OrionB-GFP is co-expressed, related to
749 Figure 3. Time-lapse movie of laser-injured ddaC dendrites from 1 to 3 hrs AI showing OrionB-
750 GFP labeling but not AV-mCard labeling on injured dendrites before fragmentation. Time stamp
751 is relative to the frame of dendrite fragmentation.

Supplementary Materials and Methods

Molecular cloning and transgenic flies

orion-mNG2$_{11x4}$-V5-T2A-LexA: Two copies of a gRNA spacer sequence targeting *orion* C-terminus and 3'UTR (Table S2) were cloned into pAC-CR7T-gRNA2.1-nlsBFP (Addgene 170515) according to published protocols (Koreman et al., 2021). The resulting plasmid was digested by PstI and NheI and assembled with four DNA fragments (through NEBuilder HiFi DNA assembly, New England Biolabs, Inc) to make an *orion* gRNA-donor vector. The four DNA fragments include a T2A-LexA-VP16 fragment that was PCR-amplified from pUC57-50-GS-FRTGFP2ALexAVP16-50 (Chen et al., 2014) (a gift from Larry Zipursky), an mNG2$_{11x4}$-V5 DNA fragment (synthesized by Integrated DNA Technologies, Inc.), and 5' and 3' homology arms (surrounding the stop codon of *orion*, ~1 kb each) that were PCR-amplified from the genomic DNA of *w^{1118}*.

UAS-orionA-GFP: OrionA coding sequence (CDS) was PCR-amplified from cDNA clone LD24308 (*Drosophila* Genomics Resource Center) and assembled with a superfolder GFP (sfGFP) fragment into pIHEU-MCS (Addgene 58375) (Sapar et al., 2018), resulting in pIHEU-orionA-GFP.

UAS-orionB-GFP: The first two exons of *orionB*, together with the first intron, was PCR-amplified from *w^{1118}* genomic DNA. The common CDS of OrionA and OrionB was PCR-amplified from LD24308. Both fragments were assembled into pIHEU-orionA-GFP to replace the orionA CDS, resulting in pIHEU-orionB-GFP.

UAS-orionB-CD2-mIFP: A pACU-CD2-mIFP plasmid was first constructed in pACU (Addgene 58373) (Han et al., 2011). The CDS of CD2-mIFP contains, from the N-terminus to the C-terminus, the rat CD2 CDS (AA24 to AA344), mIFP CDS (Yu et al., 2015), and Kir2.1 ER exit signal (Han et al., 2011). The OrionB CDS was then inserted before CD2 to make pACU-orionB-CD2-mIFP.

UAS-orionB^{AX3C}-GFP: An OrionB^{AX3C} coding fragment was amplified from pENTR-orionB-AX$_3$C (Boulanger et al., 2021) and used to replace OrionB in pIHEU-orionB-GFP, resulting in pIHEU-orionB-AX$_3$C-GFP.

UAS-orionB^{AAY}-GFP: The RRY motif in OrionB coding sequence was changed into AAY by mutagenesis PCR. The mutated OrionB fragment was used to replace OrionB in pIHEU-orionB-GFP, resulting in pIHEU-orionB-AAY-GFP.

UAS-orionB^{1}-GFP: A G611D mutation was introduced into OrionB sequence by overlap-extension PCR. The mutated OrionB fragment was used to replace OrionB in pIHEU-orionB-GFP, resulting in pIHEU-orionB-G611D-GFP.

LexAop-orionB-GFP: The OrionB-sfGFP CDS was inserted into KpnI/XbaI sites of pAPLO vector (Poe et al., 2017).

UAS-Drpr$^{\Delta Cyto}$: The extracellular domain and transmembrane domain of Drpr (AA1 to AA827) was PCR-amplified from *UAS-drpr-I* (Logan et al., 2012) genomic DNA. An smFP-HA (non-fluorescent) fragment was PCR-amplified from pCAG-smFP-HA (Viswanathan et al., 2015) (a gift from Loren Looger). The two fragments were cloned into pACU through restriction cloning, resulting in pACU-DrprTM_smGFP(dark).

UAS-smNG2$_{1-10}$: An mNG2$_{1-10}$ fragment was synthesized (Integrated DNA Technologies, Inc.) and cloned into NheI/XbaI-digested pIHEU-sfGFPLactC1C2 (Sapar et al., 2018), resulting in pIHEU-smNG2(1-10).

UAS-CDC50-T2A-ATP8A(E): The CDS of ATP8A isoform E (ATP8A(E)) was PCR-amplified from cDNA clone GH28327 (*Drosophila* Genomics Resource Center) and cloned into EcoRI/XbaI sites of pACU. The ATP8A(E) sequence is preceded by PacI and NheI sites and followed by a FLAG tag and a Kir2.1 ER exit signal (Sapar et al., 2018). In parallel, the CDC50 CDS was PCR-amplified from NB40 cDNA library (Brown and Kafatos, 1988) (a gift from Xinhua Lin) and cloned into EcoRI/XbaI sites of pACU. The CDC50 sequence is preceded by a PacI site and followed by BglII and NheI sites. A T2A fragment generated by annealed oligos was then inserted into the BglII/NheI sites. The CDC50-T2A (PacI/NheI) fragment was then released and cloned into PacI/NheI sites before ATP8A(E), resulting in pACU-CDC50-T2A-ATP8A(E).

drpr-GFP: The sfGFP CDS was inserted seamlessly before the stop codon of Drpr-PE in BAC clone CH321-16B09 according to published protocols of recombineering (Warming et al., 2005). Briefly, the *galK* CDS was first inserted before the stop codon of Drpr-PE in CH321-16B09 in bacterial strain SW102 through *galK*-mediated positive selection. The sfGFP CDS was then used to replace *galK* CDS in SW102 through *galK*-mediated negative selection. The resulting construct was transferred to bacterial strain EPI300 for propagation.

drpr-mNG: A *drpr-mNG* KI donor vector was constructed by assembling a pBluescript backbone and four DNA fragments. The four DNA fragments include the mNG CDS (Shaner et al., 2013), a 3xP3-GFP selection marker modified from pHD-DsRed (Addgene #51434), and 5' and 3' homology arms (surrounding the stop codon of Drpr-PE, ~1 kb each) that were PCR-amplified from CH321-16B09. A dual gRNA expression vector was constructed in pCFD4-U6.1_U6.3 (Port et al., 2014) to target the C-terminus and 3' UTR of *drpr* (Table S2).

gRNA-orion and *gRNA-orion-drpr*: A dual gRNA vector targeting *orion* and a quadruple gRNA vector targeting both *orion* and *drpr* were constructed in pAC-U63-QtgRNA2.1-BR (Addgene 170513) according to published protocols (Koreman et al., 2021).

Transgenic constructs were injected by Rainbow Transgenic Flies to transform flies through φC31 integrase-mediated integration into attP docker sites.

Generation of KI flies

To generate *drpr-mNG*, *drpr* KI donor vector and gRNA-expression vector were co-injected in *Act-Cas9* embryos. Adult flies from injected embryos were crossed to *w1118; TM3/TM6B*. The progeny was screened for green fluorescence in the adult eye. GFP-positive candidates were crossed to y^1 w^{67c23} *Cre(y+)*^{1b}*; D/TM3, Sb*^{1} (BDSC, #851) to remove 3xP3-GFP. GFP-negative candidates were made isogenic and the mNG insertion was confirmed by genomic PCR and sequencing.

To generate *orion-mNG2*$_{11x4}$*-V5-T2A-LexA*, the *orion* gRNA-donor vector was injected into y^1 *nos-Cas9*$^{ZH-2A}$ w^* (BDSC, #54591) embryos. Adult flies from injected embryos were crossed to y^1 w^**; 13XLexAop2-6XGFP*^{attP2}*/TM6B* (BDSC, #52266). GFP-positive female candidates from the progeny were collected to cross with y^1 w^**; TM3/TM6B*. The adult progeny was then screened for GFP-positive males that were white-eyed and RFP-negative (i.e. having no *nos-Cas9*$^{ZH-2A}$). The males were then crossed to FM6 to remove *13XLexAop2-6XGFP*^{attP2} and to

establish isogenic stocks. The -mNG211x4-V5-T2A-LexA insertion is verified by genomic PCR and sequencing.

CRISPR-TRiM

The efficiency of transgenic gRNA lines was validated by the Cas9-LEThAL assay (Poe et al., 2019). Homozygous males of each gRNA line were crossed to *Act-Cas9 w lig4* (BDSC, #58492) homozygous females. *gRNA-orion* crosses yielded viable female progeny and male lethality between 3rd instar larvae to prepupae; *gRNA-drpr* crosses resulted in lethality in late pupae; *gRNA-orion-drpr* crosses yielded viable female progeny and male lethality before wandering 3rd instar larvae. These results suggest that all gRNAs are efficient.

C4da-specific gene knockout was carried out using *ppk-Cas9* (Poe et al., 2019). Tissue-specific knockout in da neuron precursor cells was carried out with *SOP-Cas9* (Poe et al., 2019). Tissue-specific knockout in pan-epidermal cells was carried out using *shot-Cas9* (Ji et al., 2022). Tissue-specific knockout in epidermal cells in the posterior half of each segment was carried out using *hh-Cas9* (Poe et al., 2019). Whole-animal knockout was carried out using *Act-Cas9* (Port et al., 2014).

Live imaging

Animals were reared at 25°C in density-controlled vials (60-100 embryos/vial) on standard yeast-glucose medium (doi:10.1101/pdb.rec10907). Larvae at 96 hours AEL (3rd instar larval stage) or stages specified were mounted in 100% glycerol under coverslips with vacuum grease spacers and imaged using a Leica SP8 microscope equipped with a 40X NA1.30 oil objective. Larvae were lightly anesthetized with isoflurane before mounting. For consistency, we imaged dorsal ddaC neurons from A1-A3 segments (2-3 neurons per animal) on one side of the larvae. Unless stated otherwise, confocal images shown in all figures are maximum intensity projections of z stacks encompassing the epidermal layer and the sensory neurons beneath, which are typically 8–10 μm for 3rd instar larvae.

Injury assay

Injury assay at the larval stage was done as described previously (Sapar et al., 2018). Briefly, larvae at 84 hrs AEL were lightly anesthetized with isoflurane, mounted in a small amount of halocarbon oil under coverslips with grease spacers. The laser ablation was performed on a Zeiss LSM880 Confocal/Multiphoton Upright Microscope, using a 790 nm two-photon laser at primary dendrites of ddaC neurons in A1 and A3 segments. Animals were recovered on grape juice agar plates following lesion for appropriate times before imaging.

Long-term time-lapse imaging

Long-term time-lapse imaging at the larval stage was done as described previously (Ji et al., 2022; Sapar et al., 2018). Briefly, a layer of double-sided tape was placed on the coverslip to define the position of PDMS blocks. A small amount of UV glue was added to the groove of PDMS and to the coverslip. Anesthetized larvae were placed on top of the UV glue on the coverslip and then covered by PDMS blocks with the groove side contacting the larva. Glue was then cured by 365nm UV light. The coverslip with attached PDMS and larvae was mounted on an aluminum slide chamber that contained a piece of moistened Kimwipes (Kimtech Science) paper. Time-lapse imaging was performed on a Leica SP8 confocal equipped with a 40x NA1.3 oil objective and a resonant scanner at digital zoom 0.75 and a 3-min interval. For imaging after

ablation, larvae were pre-mounted in the imaging chamber and subjected to laser injury. The larvae were then imaged 1-2 hours after ablation.

Pinching assay

Larvae at 96 hrs AEL were lightly anesthetized with isoflurane. Gentle pinching was performed at A2 or A3 segment and near the dorsal midline of larvae using a pair of forceps (DUMONT # 3, Fisher Scientifics) without cracking the cuticle. The pinched larvae were imaged after a 2-hr recovery.

Immunohistochemistry

Immunostaining of *Drosophila* larvae was performed as previously described (Poe et al., 2017). Briefly, 3rd instar larvae were dissected in cold PBS, fixed in 4% formaldehyde/PBS for 20 min at room temperature, and stained with the proper primary antibodies (Table S1) for 2 hrs at room temperature and subsequent secondary antibodies (Table S1) for 2 hrs at room temperature.

Image analysis and quantification

Image processing and analyses were done in Fiji/ImageJ or ilastik. For injured dendrites and pruned dendrites marked by *ppk-MApHS*, the pHluorin-positive pixel area in a region of interest (ROI) (ApH), tdTom positive pixel area in the ROI (Atom) were measured and the unengulfment ratio was calculated based on following formula: 100·ApH/Atom. Methods for tracing and measuring C4da neuron dendrite length have been previously described (Poe et al., 2017). Briefly, the images were segmented by Auto Local Threshold and reduced to single pixel skeletons before measurement of skeleton length by pixel distance. The dendrite debris measurement has been described previously (Sapar et al., 2018). Briefly, a region of interest (ROI) was generated by including a quadrant of a neuron's territory. Dendrite debris within the ROI was converted to binary masks based on fixed thresholds. Different thresholds were used for *ppk-C4-tdTom* and *ppk-Gal4 UAS-CD-tdTom* as they have different brightness. The debris pixel area (Adeb), and ROI area (AROI) were measured, and dendrite coverage ratio was calculated based on following formula: 100·ADeb/AROI. For measuring debris dispersion of injured dendrites, dendrite debris was segmented by Auto Threshold (the "Default" method) in a rectangular ROI that was previously covered by injured dendrites. The ROI was divided into 15X15-pixel squares. The debris spread index was the area ratio of all squares containing dendrite debris in the ROI. For measuring Orion-GFP and AV-mCard on dendrites, tdTom signals on dendrites were used to generate dendrite masks for measurement of GFP or mCard mean intensities within the masks. For measuring Drpr-GFP recruitment, tdTom signals on dendrites were used to generate dendrite masks to measure total dendrite area (Atot) and GFP-positive area (AGFP). The Drpr recruitment index was calculated based on the formula: AGFP/Atot. For V5 staining, Drpr staining and Orion-GFP binding on epidermal cells, signals on cell boundaries of epidermal cells were measured. For Orion-GFP variant intensities in hemolymph, the signal in a single optical section was measured. For Orion-GFP variant intensities in fat body, maximum projected image was measured.

Statistical Analysis

R was used to conduct statistical analyses and generate graphs. (*$p < 0.05$, **$p < 0.01$, and ***$p < 0.001$). Statistical significance was set at $p < 0.05$. Data acquisition and quantification were performed non-blinded. Acquisition was performed in ImageJ. Statistical analyses were performed using R. We used the following R packages: car, stats, multcomp for statistical

analysis and ggplot2 for generating graphs. For the statistical analysis we ran the following tests, ANOVA (followed by Tukey's HSD) when dependent variable was normally distributed and there was approximately equal variance across groups. When dependent variable was not normally distributed and variance was not equal across groups, we used Kruskal-Wallis (followed by Dunn's test, p-values adjusted with Benjamini-Hochberg method) to test the null hypothesis that assumes that the samples (groups) are from identical populations. We used Welch's t-test for comparison between two groups. To check whether the data fit a normal distribution, we generated qqPlots to analyze whether the residuals of the linear regression model are normally distributed. We used the Levene's test to check for equal variance within groups. The quantification of percentages of injured dendrites showing different timings of AV binding was compared using Fisher's exact test.

Replication

For all larval and adult imaging experiments, at least 3 biological replications were performed for each genotype and/or condition.

Table S1. Key Resource Table

REAGENT or RESOURCE	SOURCE	IDENTIFIER	ADDITIONAL INFORMATION
Experimental Models: Organisms/Strains			
orion^{1}	(Boulanger et al., 2021)		
orion$^{\Delta C}$	(Boulanger et al., 2021)		
orion$^{\Delta A}$	(Boulanger et al., 2021)		
orion$^{\Delta B}$	(Boulanger et al., 2021)		
orion-mNG2$_{11x4}$*-V5-T2A-LexA (orion*^{KI}*)*	this study		*orion-mNG(11x4)-F2A-LexA::VP16*$^{7A-1}$
Act5C-Cas9	Bloomington Drosophila Stock Center	RRID:BDSC _54590	*Act5C-Cas9.P*
ppk-MApHS	(Han et al., 2014)		*ppk-MApHS*^{1}
UAS-TMEM16F	(Sapar et al., 2018)		*UAS-TMEM16F(D430G)*^{VK00016}
ppk-Gal4	(Han et al., 2012)		*ppk-Gal4*^{VK00037}
21-7-Gal4	(Song et al., 2007)		*GawB*$^{21-7}$
Dcg-Gal4	(Suh et al., 2006)		
UAS-AnnexinV-mCard	(Sapar et al., 2018)		*UAS-AnnexinV-mCard*^{VK00037}
UAS-CD4-tdTom	(Han et al., 2011)		*UAS-CD4-tdTom*^{7M1}
UAS-OrionB-GFP	this study		*UAS-orion(B)-sfGFP*^{VK00018}
UAS-OrionB-Myc	(Boulanger et al., 2021)		*UAS-orion-B-myc*

UAS-CDC50-T2A-ATP8A(E)	this study		*UAS-CDC50-T2A-ATP8A(E)*^{VK00016}
LexAop-OrionB-GFP	this study		*LexAop-orion(B)-sfGFP*^{VK37}
ppk-Cas9	(Poe et al., 2019)		*ppk-Cas9*^{7D}
UAS-Drpr	Bloomington Drosophila Stock Center	RRID:BDSC_67035	*UAS-drpr[I]*
drpr-GFP	this study		*drpr-sfGFP*^{VK00037}
Dcg-LexA	this study		
UAS-Drpr^{Cyto}	this study		*UAS-drprTM-smGFP.HA*^{VK00018}
UAS-OrionB-CD2-mIFP	this study		*UAS-Orion(B)-CD2-mIFP*^{VK00019}
UAS-ATP8A	(Ji et al., 2022)		*UAS-ATP8Acore*^{VK00016}
UAS-OrionB^{AX3C}*-GFP*	this study		*UAS-orion(B.CX3Cmut)-sfGFP*^{VK00018}
UAS-OrionB^{AAY}*-GFP*	this study		*UAS-orion(B.RRYmut)-sfGFP*^{VK00018}
UAS-OrionB^{1}*-GFP*	this study		*UAS-orion(B.G611D)-sfGFP*^{VK00018}
UAS-AVmut-GFP	(Sapar et al., 2018)		*UAS-AnnexinV(mut)-GFP*^{VK00018}
ppk-Cas9	(Poe et al., 2019)		*ppk-Cas9*^{7D}
gRNA-CDC50	(Sapar et al., 2018)		*gRNA-CDC50*^{attP2}
gRNA-Nmnat	(Ji et al., 2022)		*gRNA-NmnatVK00027*
LexAop-GFPnls	Bloomington Drosophila Stock Center	RRID:BDSC _29955	*lexAop-2xhrGFP.nls*^{3a}
gRNA-orion	this study		*gRNA-orion(BR)*^{VK00027}
shot-Cas9	(Ji et al., 2022)		*shot-Cas9*^{1A}
SOP-Cas9	(Poe et al., 2019)		*[sc-E1]x8-Cas9*^{3A}
R16D01-Gal4	Bloomington Drosophila Stock Center	RRID: BDSC_48722	*R16D01-Gal4*^{attP2}
UAS-smNG$_{1-10}$	this study		*UAS-smNG2(1-10)*^{VK00027}
ppk-LexA	(Poe et al., 2017)		*ppk-LexA.GAD*^{3}
LexAop-Wld^{S}	(Ji et al., 2022)		*LexAop-WldS*^{VK00027}
ppk-CD4-tdTom	(Han et al., 2011)		*ppk-spGFP11-CD4-tdTom*^{2}
R16A03-LexA	(Sapar et al., 2018)		*R16A03-LexAp65*^{VK00027}

UAS-mIFP-T2A-HO1	(Poe et al., 2017)	RRID: BDSC_64181	*UAS-mIFP-T2A-HO1*^{VK00005}
UAS-GFP-LactC1C2	(Sapar et al., 2018)		*UAS-GFP-LactC1C2*^{VK00018}
drpr^{-}	(Sapar et al., 2018)		*drpr*^{indel3}
gRNA-drpr	(Ji et al., 2022)		*gRNA-drpr(BR)*^{VK00027}
gRNA-orion-drpr	this study		*gRNA-orion-drpr(BR)*^{VK00027}
hh-Cas9	(Poe et al., 2019)		*R28E04-Cas9*^{6A}
drpr-mNG	this study		*drpr-mNeonGreen*$^{1008-15}$
UAS-Drpr	(Logan et al., 2012)		*UAS-drpr[I]:HA*
R38F11-Gal4	Bloomington Drosophila Stock Center	RRID: BDSC_50014	*R38F11-Gal4*^{attP2}
gRNA-ATP8A	(Sapar et al., 2018)		*gRNA-ATP8A*^{VK00019}
hh-Gal4	(Han et al., 2004)		
Dp(1:3)DC496	Bloomington Drosophila Stock Center	RRID:BDSC_33489	*PBac{DC496}*^{VK00033}
ppk-Gal4	(Han et al., 2012)		*ppk-Gal4*^{1a}
UAS-CD4-tdTom	(Han et al., 2011)		*UAS-CD4-tdTom*^{VK00033}
y^{1} *w*^{67c23} *Cre(y+)*^{1b}*; D/TM3, Sb*^{1}	Bloomington Drosophila Stock Center	RRID:BDSC_851	
y^{1} *nos-Cas9*$^{ZH-2A}$ *w**	Bloomington Drosophila Stock Center	RRID:BDSC_54591	
13XLexAop2-6XGFP	Bloomington Drosophila Stock Center	RRID:BDSC_52266	*13XLexAop2-6XGFP*^{attP2}
Act-Cas9 w lig4	Bloomington Drosophila Stock Center	RRID:BDSC_58492	*y*^{1} *Act5C-Cas9(RFP-)*$^{ZH-2A}$ *w*^{1118} *DNAlig4*^{169}
Recombinant DNA			
pAC-CR7T-gRNA2.1-nlsBFP	(Koreman et al., 2021)	RRID:Addgene_170515	
pUC57-50-GS-FRTGFP2ALexAVP16-50	(Chen et al., 2014)		
LD24308	*Drosophila* Genomics Resource Center		
pIHEU-MCS	(Sapar et al., 2018)	RRID:Addgene_58375	
pACU	(Han et al., 2011)	RRID:Addgene_58373	
pENTR-orionB-AX3C	(Boulanger et al., 2021)		
pAPLO	(Poe et al., 2017)	RRID:Addgene_112805	

pCAG-smFP-HA	(Viswanathan et al., 2015)	RRID:Addgene_59759	
GH28327	*Drosophila* Genomics Resource Center		
NB40 cDNA library	(Brown and Kafatos, 1988)		
CH321-16B09	BACPAC Resources Center		
pGalK	(Warming et al., 2005)		
pHD-DsRed	Addgene	RRID:Addgene_51434	
pCFD4-U6.1_U6.3	(Port et al., 2014)	RRID:Addgene_49411	
pAC-U63-QtgRNA2.1-BR	(Koreman et al., 2021)	RRID:Addgene_170513	
Bacterial Strains			
SW102	(Warming et al., 2005)		
EPI300	Lucigen Corporation	Cat. # C300C105	
Antibody			
Rat-Elav-7E8A10 (1:20)	Developmental Studies Hybridoma Bank	AB_528218	
8D12 anti-Repo (1:20)	Developmental Studies Hybridoma Bank	AB_528448	
V5 Tag Antibody (R960-25) (1:400)	Thermo Fisher Scientific	AB_2556564	
Rabbit anti Drpr polyclonal (1:100)	(Freeman et al., 2003)		
Cy™5 AffiniPure Donkey Anti-Rat IgG (H+L) (1:200)	Jackson ImmunoResearch Labs	AB_2340671	712-175-150
Alexa Fluor® 647 AffiniPure Donkey Anti-Mouse IgG (H+L) (1:200)	Jackson ImmunoResearch Labs	RRID: AB_2340862	715-605-150
Alexa Fluor® 488 AffiniPure Donkey Anti-Rabbit IgG (H+L) (1:200)	Jackson ImmunoResearch Labs	RRID: AB_2313584	711-545-152
Alexa Fluor® 488 AffiniPure Donkey Anti-Mouse IgG (H+L) (1:400)	Jackson ImmunoResearch Labs	RRID: AB_2340846	715-545-150
Software and Algorithms			
Fiji	https://fiji.sc/	RRID: SCR_002285	
R	https://www.r-project.org/	RRID: SCR_001905	

Adobe Photoshop	Adobe	RRID:SCR_014199	
Adobe Illustrator	Adobe	RRID:SCR_010279	
ilastik	(Berg et al., 2019)		
AlphaFold2.ipynb	(Mirdita et al., 2021)		
UCSF Chimera	(Pettersen et al., 2004)		
Other			
NEBuilder® HiFi DNA Assembly Master Mix	New England Biolabs Inc.	#E2621	

Table S2. gRNA target sequences.

Gene	Target sequence 1	Target sequence 2
orion (for KO)	GAAGGGCAACTACACCCAGG	CATGTTTCGTCGGATCACAG
orion (for KI)	GATTCTAAAGCGGAGAGAAG	
drpr (for KO)	CCATGCCGTAGAATCCAGGT	ACGGACAAGGATGCGCCCAG
drpr (for KI)	AGAAATTTCGGACTGGAACT	GCCGGAACAGTCACTTCACC

Reference

Berg, S., Kutra, D., Kroeger, T., Straehle, C.N., Kausler, B.X., Haubold, C., Schiegg, M., Ales, J., Beier, T., Rudy, M., *et al.* (2019). ilastik: interactive machine learning for (bio)image analysis. Nat Methods *16*, 1226-1232.

Boulanger, A., Thinat, C., Zuchner, S., Fradkin, L.G., Lortat-Jacob, H., and Dura, J.M. (2021). Axonal chemokine-like Orion induces astrocyte infiltration and engulfment during mushroom body neuronal remodeling. Nat Commun *12*, 1849.

Brown, N.H., and Kafatos, F.C. (1988). Functional cDNA libraries from Drosophila embryos. J Mol Biol *203*, 425-437.

Chen, Y., Akin, O., Nern, A., Tsui, C.Y., Pecot, M.Y., and Zipursky, S.L. (2014). Cell-type-specific labeling of synapses in vivo through synaptic tagging with recombination. Neuron *81*, 280-293.

Freeman, M.R., Delrow, J., Kim, J., Johnson, E., and Doe, C.Q. (2003). Unwrapping glial biology: Gcm target genes regulating glial development, diversification, and function. Neuron *38*, 567-580.

Frost, J.L., and Schafer, D.P. (2016). Microglia: Architects of the Developing Nervous System. Trends Cell Biol *26*, 587-597.

Han, C., Belenkaya, T.Y., Wang, B., and Lin, X. (2004). Drosophila glypicans control the cell-to-cell movement of Hedgehog by a dynamin-independent process. Development *131*, 601-611.

Han, C., Jan, L.Y., and Jan, Y.N. (2011). Enhancer-driven membrane markers for analysis of nonautonomous mechanisms reveal neuron-glia interactions in Drosophila. Proc Natl Acad Sci U S A *108*, 9673-9678.

Han, C., Song, Y., Xiao, H., Wang, D., Franc, N.C., Jan, L.Y., and Jan, Y.N. (2014). Epidermal cells are the primary phagocytes in the fragmentation and clearance of degenerating dendrites in Drosophila. Neuron *81*, 544-560.

Han, C., Wang, D., Soba, P., Zhu, S., Lin, X., Jan, L.Y., and Jan, Y.N. (2012). Integrins regulate repulsion-mediated dendritic patterning of drosophila sensory neurons by restricting dendrites in a 2D space. Neuron *73*, 64-78.

Ji, H., Sapar, M.L., Sarkar, A., Wang, B., and Han, C. (2022). Phagocytosis and self-destruction break down dendrites of Drosophila sensory neurons at distinct steps of Wallerian degeneration. Proceedings of the National Academy of Sciences *119*, e2111818119.

Koreman, G.T., Xu, Y., Hu, Q., Zhang, Z., Allen, S.E., Wolfner, M.F., Wang, B., and Han, C. (2021). Upgraded CRISPR/Cas9 tools for tissue-specific mutagenesis in Drosophila. Proc Natl Acad Sci U S A *118*.

Logan, M.A., Hackett, R., Doherty, J., Sheehan, A., Speese, S.D., and Freeman, M.R. (2012). Negative regulation of glial engulfment activity by Draper terminates glial responses to axon injury. Nat Neurosci *15*, 722-730.

Mirdita, M., Schütze, K., Moriwaki, Y., Heo, L., Ovchinnikov, S., and Steinegger, M. (2021). ColabFold - Making protein folding accessible to all. bioRxiv, 2021.2008.2015.456425.

Pettersen, E.F., Goddard, T.D., Huang, C.C., Couch, G.S., Greenblatt, D.M., Meng, E.C., and Ferrin, T.E. (2004). UCSF Chimera--a visualization system for exploratory research and analysis. J Comput Chem *25*, 1605-1612.

Poe, A.R., Tang, L., Wang, B., Li, Y., Sapar, M.L., and Han, C. (2017). Dendritic space-filling requires a neuronal type-specific extracellular permissive signal in Drosophila. Proc Natl Acad Sci U S A *114*, E8062-E8071.

Poe, A.R., Wang, B., Sapar, M.L., Ji, H., Li, K., Onabajo, T., Fazliyeva, R., Gibbs, M., Qiu, Y., Hu, Y., *et al.* (2019). Robust CRISPR/Cas9-Mediated Tissue-Specific Mutagenesis Reveals Gene Redundancy and Perdurance in Drosophila. Genetics *211*, 459-472.

Port, F., Chen, H.M., Lee, T., and Bullock, S.L. (2014). Optimized CRISPR/Cas tools for efficient germline and somatic genome engineering in Drosophila. Proc Natl Acad Sci U S A *111*, E2967-2976.

Sapar, M.L., Ji, H., Wang, B., Poe, A.R., Dubey, K., Ren, X., Ni, J.Q., and Han, C. (2018). Phosphatidylserine Externalization Results from and Causes Neurite Degeneration in Drosophila. Cell Rep *24*, 2273-2286.

Shaner, N.C., Lambert, G.G., Chammas, A., Ni, Y., Cranfill, P.J., Baird, M.A., Sell, B.R., Allen, J.R., Day, R.N., Israelsson, M., *et al.* (2013). A bright monomeric green fluorescent protein derived from Branchiostoma lanceolatum. Nat Methods *10*, 407-409.

Song, W., Onishi, M., Jan, L.Y., and Jan, Y.N. (2007). Peripheral multidendritic sensory neurons are necessary for rhythmic locomotion behavior in Drosophila larvae. Proc Natl Acad Sci U S A *104*, 5199-5204.

Suh, J.M., Gao, X., McKay, J., McKay, R., Salo, Z., and Graff, J.M. (2006). Hedgehog signaling plays a conserved role in inhibiting fat formation. Cell Metab *3*, 25-34.

Viswanathan, S., Williams, M.E., Bloss, E.B., Stasevich, T.J., Speer, C.M., Nern, A., Pfeiffer, B.D., Hooks, B.M., Li, W.P., English, B.P., *et al.* (2015). High-performance probes for light and electron microscopy. Nat Methods *12*, 568-576.

Warming, S., Costantino, N., Court, D.L., Jenkins, N.A., and Copeland, N.G. (2005). Simple and highly efficient BAC recombineering using galK selection. Nucleic Acids Res *33*, e36.

Yu, D., Baird, M.A., Allen, J.R., Howe, E.S., Klassen, M.P., Reade, A., Makhijani, K., Song, Y., Liu, S., Murthy, Z., *et al.* (2015). A naturally monomeric infrared fluorescent protein for protein labeling in vivo. Nat Methods *12*, 763-765.